K Further Contributions

articles available on-line: http://www.fz-juelich.de/ikp/DE/Service/Download/download_node.html

- Analyzing Power of Proton, Kaon, and Lambda in the $\vec{p}p \to pK\Lambda$ Reaction at 2.7 GeV/c
- Developing a Free-Running Readout ASIC for the MVD Strip Sensors
- Simulated Measurement of the D_s Semileptonic Decay Form Factor with the $\overline{\text{P}}$ANDA Detector
- GPU-based Online Tracking Algorithms for the PANDA Experiment
- FEE-free signal processing system for PANDA Straw Tube Tracker
- Test Beam with a PANDA Trapezoidal Prototype Sensor
- Data Analysis of the KOALA Experiment Commissioning at COSY
- Search for polarization effects in the antiproton production process
- Measurement of the analyzing power in $p(pol)d$ elastic scattering at small angles
- The quasi-free reaction $pd \to d + \eta + p_{sp}$ close to threshold at ANKE
- Luminosity determination via dp-elastic scattering at ANKE
- The quasi-free pn-elastic scattering measurements at ANKE
- Investigation of Dipion Final State Interactions in $pp \to pp\eta[\eta \to \pi^+\pi^-\gamma]$ with WASA-at-COSY
- Charge symmetry breaking in the $dd \to {}^4\text{He}\pi^0$ reaction with the WASA-at-COSY experiment
- Investigation of total cross section structures in the $pd \to {}^3\text{He}\eta$ reaction with WASA-at-COSY
- Search for C-violation in the Decay $\eta \to \pi^0 e^+ e^-$ at WASA-at-COSY
- Studying the reaction $pd \to {}^3\text{He}\pi^0$ with WASA-at-COSY
- ToPix 4 Readout System and Test Beam Measurements
- Systematic studies of spin dynamics at COSY in preparation for the EDM searches
- Systematic error investigation of the spin tune analysis for an EDM measurement at COSY
- Development of a new control framework for lattice parameter calculations and particle tracking
- Wien filter studies in MODE
- Upgrade of the Low Energy Polarimeter read-out
- Data Interface between COSY and EDDA-DAQ System
- Beam Position Monitors for the HESR
- Upgrade of the beam profile monitoring system in the COSY IBL
- Automated Compensation of Larmor Rotation in the 2 MeV Electron Cooler
- An RF Wien-filter for EDM Searches at COSY

Analyzing Power of Proton, Kaon, and Lambda in the $\vec{p}p \to pK\Lambda$ Reaction at 2.7 GeV/c

Florian Hauenstein, for the COSY-TOF collaboration

The $\vec{p}p \to pK^+\Lambda \to pK^+p\pi^-$ reaction was measured with the COSY-TOF detector using a polarized proton beam with 2.7 GeV/c momentum. The beam polarization was measured to be (79.0 ± 1.1) % [3] from the analysis of proton-proton elastic scattered events. Using this polarization the analyzing power of the final state particles (proton, Λ and kaon) was determined. Especially, the kaon analyzing power is important for the further extraction of the spin triplet $p\Lambda$ scattering length (see [3]). Furthermore, all analyzing powers can be used in a dedicated analysis to disentangle the various contributions to the production mechanism of the reaction. This can be done for example by a partial wave analysis (PWA).

The analyzing power for each particle is determined by the measured left-right azimuthal asymmetry and the beam polarization p_B according to:

$$A_N(\cos\theta_X^{\mathrm{CMS}}) = \frac{\epsilon_{LR}(\cos(\theta_X^{\mathrm{CMS}}), \phi_X)}{\cos(\phi_X) \cdot p_B} \tag{1}$$

with $X = p, K, \Lambda$ being the particle of interest. ϵ_{LR} is the left-right azimuthal asymmetry given by

$$\epsilon_{LR}(\theta_X^{\mathrm{CMS}}, \phi_X) = \frac{L(\theta_X^{\mathrm{CMS}}, \phi_X) - R(\theta_X^{\mathrm{CMS}}, \phi_X)}{L(\theta_X^{\mathrm{CMS}}, \phi_X) + R(\theta_X^{\mathrm{CMS}}, \phi_X)} \tag{2}$$

with

$$L(\theta_X^{\mathrm{CMS}}, \phi_X) = \sqrt{N^+(\phi) \cdot N^-(\phi + \pi)} \tag{3}$$

$$\text{and} \quad R(\theta_X^{\mathrm{CMS}}, \phi_X) = \sqrt{N^+(\phi + \pi) \cdot N^-(\phi)} \tag{4}$$

similar to the method for the determination of the beam polarization (see [2, 3]). $N^{\pm}(\phi)$ are the number of events for the azimuthal angle ϕ with a spin up (+) or spin down (−) polarized beam, respectively. Multiplying the number of events on one detector side with the number of events on the other side with opposite spin cancels out systematic effects from an azimuthal asymmetric detector acceptance to first order.

The results for the analyzing power as a function of $\cos(\theta_X^{\mathrm{CMS}})$ are shown in Figure 1 (upper: proton, middle: Λ, lower: kaon). For $\cos(\theta_X^{\mathrm{CMS}}) = \pm 1$ the analyzing power has to be zero since the ϕ angle is not defined there, thus the asymmetry ϵ_{LR} is zero. Each analyzing power is fit with the sum of the associated Legendre polynomials $P_1^1(\cos\theta) = -\sin\theta$ and $P_2^1(\cos\theta) = -3\cos\theta\sin\theta$. These are the polynomials of order $m = 1$ with the lowest angular momentum. The total fit is shown by the red lines in the plots in Figure 1. The individual contributions of the Legendre polynomials P_1^1 and P_2^1 are indicated by the green dashed and blue dashed lines, respectively. In addition, the χ^2 value of the fits and the fit parameters α and β which are the magnitudes of the individual P_l^m contributions are given.

The proton analyzing power is well described by the fit with a reduced χ^2 value of 1.01 (Figure 1 upper). This indicates that the highest order of the proton partial wave is probably $l = 2$ (D-wave).

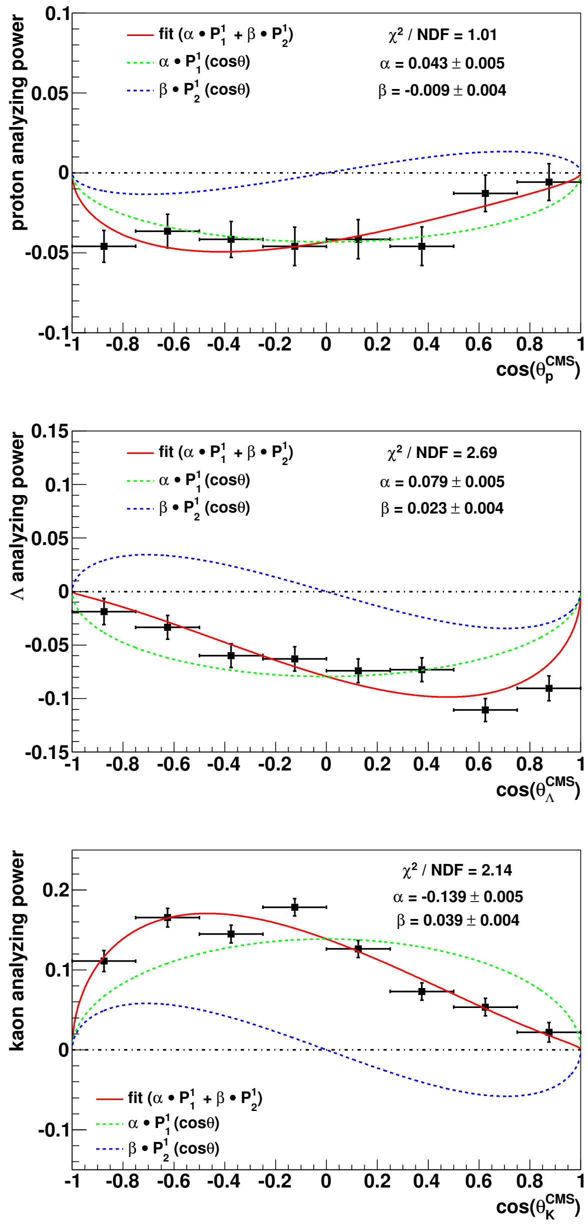

Fig. 1: Analyzing power A_N for the final state particles (upper: proton, middle: Λ, lower: kaon) as a function of $\cos(\theta^{\mathrm{CMS}})$. The red line in each plot shows the fit with a sum of the two associated Legendre polynomials P_1^1 and P_2^1. The individual contributions of the polynomials are shown by the green dashed and blue dashed lines in each plot, respectively.

However, in case of the Λ analyzing power the reduced χ^2 value of the fit is 2.69 (Figure 1 middle). As shown in [3], an inclusion of the next order Legendre polynomial P_3^1 into the fit improves the reduced χ^2 value to 1.40. Therefore, the Λ has presumably higher order partial wave contributions than D-wave.

The fit of the kaon analyzing power gives a reduced χ^2 value of 2.14 (Figure 1 lower). In this case, including higher order Legendre polynomials does not improve the fit further. Therefore, the kaon analyzing power distribution is described by the two parameters α and β. The contribution of the symmetric Legendre polynomial P_1^1 is used for the determination of the spin triplet $p\Lambda$ scattering length. The description of the determination procedure and the results can be found in [3].

References:

[1] M. Roeder, PhD Thesis, University Bochum, 2011.
[2] F. Hauenstein, IKP Annual Report, 2013.
[3] F. Hauenstein, PhD Thesis, University Erlangen, 2014.

Developing a Free-Running Readout ASIC for the MVD Strip Sensors

A. Goerres, Forschungszentrum Jülich

Introduction The Anti-Proton Annihilation at Darmstadt ($\overline{\text{P}}$ANDA) experiment is one of the main experiments at the Facility for Antiproton and Ion Research (FAIR), which is under construction in Darmstadt. $\overline{\text{P}}$ANDA's innermost part is the Micro Vertex Detector (MVD) with silicon pixel and strip sensors. The experiment's concept of a trigger-less operation requires a free-running readout solution, which should be capable of processing events up to 40 kHz/channel in hot spots of the strip part. Events will need an accurate time (<10 ns) and charge (resolution: 8 bit) information, while using less than 4 mW per channel (requirements from [1]). Because of the given requirements, a simple architecture especially for the analog domain has to be used.
A predecessor application specific integrated circuit (ASIC) has been developed for a medical application reading out silicon photomultipliers in a PET scanner [2]. The concept has been proven to be precise in timing (110 ps RMS for a single photon at 160 MHz clock input frequency) while having only low power consumption at around 8 mW per channel [3]. With the gained knowledge from this TOFPET ASIC and the necessary changes towards reading out silicon strip sensors, a first PASTA prototype has been developed to match the given requirements.

The $\overline{\text{P}}$ANDA Strip ASIC's Concept The basic concept of the $\overline{\text{P}}$ANDA Strip ASIC (PASTA) relies on leading-edge discriminators, providing time information for the crossing of a threshold from the input signal. With that, the time of arrival on the leading edge of the pulse is measured as well as the pulse length with a second point on the falling edge. The latter gives a time over threshold which is correlated with the collected charge and thus represents a measurement thereof.
Two discriminators with independent threshold levels are used to fulfill two goals: A precise time of arrival measurement is done with a low threshold ($V_{\text{th\_T}}$) to minimize the effect of time walk[1]. The second, higher threshold ($V_{\text{th\_E}}$) ensures a stable time over threshold measurement because noise fluctuations on the signal have less impact on the time jitter when the slope is steep (see Figure 1).

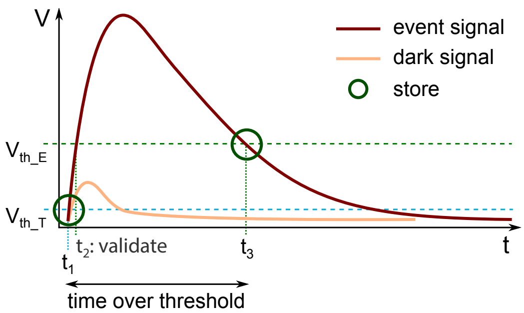

Fig. 1: A simplified signal after the pre-amplifier. Two discriminator levels deliver four points in time, t_1 and t_3 are stored in the default operation mode for the time of arrival and the time over threshold. Only if the signal exceeds $V_{\text{thr\_E}}$ it is processed.

[1]One is interested in the true starting time of the signal. Increasing the threshold will lead to delayed time measurements because of the pulse's slope. This phenomenon is called time walk.

The nominal operation frequency of the chip is 160 MHz, therefore it delivers an intrinsic digital timing resolution of 6.25 ns. To get a finer resolution, a time interpolation is performed. This is obtained by discharging a capacitor with a constant current for the time between the discriminator trigger and the clock edge. In this step the time is transformed into a proportional voltage difference. After transferring the charge to a bigger capacitor and recharging with a lower but still constant current, an amplification of 128 is reached. For the same clock speed, this leads to a binning of 50 ps of this fine time measurement. The downside of this technique is an introduced dead time but according to simulations, a continuous rate of up to 100 kHz per channel is achievable, which is well above the expected event rate.

Recent Developments While the main aspects of the development in the digital part has been reported in last year's report already [4], their finalization continued in 2014. This regards especially the completion of the newly designed control logic for data taking as well as the protection for radiation effects in the whole digital design.
Besides the digital part, also an analog block is being developed from the INFN Torino group. To minimize the influence from digital switching activity to the extremely high sensitive amplifiers in the analog domain, a separation wherever possible is desired. Thus, the bulk connections of transistors in the digital part get an individual supply connections (`VBN`) instead of short-circuiting them to their source (`VSS`).

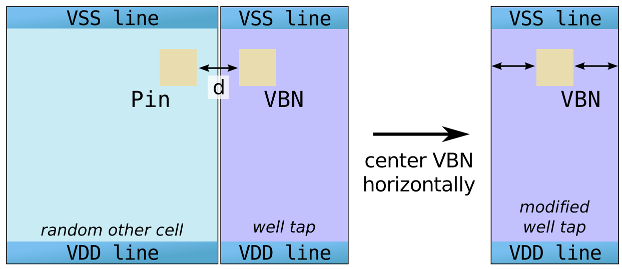

Fig. 2: The bulk connection pin (`VBN`) is placed left aligned so that the distance to an adjacent pin (d) is minimal. The modified cell has this pin horizontally centered to relax the narrow spacing.

The provided cells for such a purpose are called *well tap* cells. Their geometrical definition aligns the bulk connection pin (`VBN`) to the left side in a way, that an adjacent cell with a pin on the same height would have the minimal allowed distance d in between (see Figure 2). In some placing scenarios the routing conditions requires additional structures[2], reducing the distance below the given constraint. A modification in the library by centering this pin solved the problem and enabled a successful routing.
Aiming at a final design, digital and analog parts have been combined and simulations performed to verify a proper functionality. This leads to a layout with an input channel pitch of

[2]If routing cannot be done in the same metal layer, a via is used to change layers. The via's area needs to be slightly larger than the area of a pin, which consequently decreases the spacing to the adjacent cell's pin.

$63.8\,\mu$m for 64 channels and an expected power consumption of less than 4 mW per channel.
In parallel to the ASIC's development, an adaptation of the readout system for ASICs, developed in the IKP's MVD group, towards PASTA has started. This includes the preparation for the expected event and configuration data format as well as the specifics of data transmission. My DAAD summer student A. Mahler contributed to this by implementing an 8b/10b decoder into the system's firmware. Furthermore he worked on the user control software and created a configuration interface as well as a parser for the incoming data stream.

Outlook Final checks of the ASIC have to be done to verify a fully functional design which will be submitted to the ASIC foundry early 2015. Thorough testing of the prototype will follow, involving the afore-mentioned readout system whose adaptation to the PASTA interface has to be finished as well.

References:

[1] The $\overline{\text{P}}$ANDA Collaboration, *Technical Design Report for the: PANDA Micro Vertex Detector*. (2011) http://arxiv.org/abs/1207.6581

[2] Rolo, M. D. et al, *TOFPET ASIC for PET applications*. *Journal of Instrumentation* (2013) 1748. http://dx.doi.org/10.1088/1748-0221/8/02/C02050

[3] Bugalho, R. et al, *Design and Performance of an ASIC for TOF applications*. *Nuclear Science Symposium and Medical Imaging Conference (NSS/MIC), 2013 IEEE* (2013). http://dx.doi.org/10.1109/NSSMIC.2013.6829772

[4] Goerres, A, *Adapting the TOFPET Readout ASIC for the MVD Strip Sensors*. *Annual Report 2013 - Short Contributions*.

Simulated Measurement of the Ds Semileptonic Decay Form Factor with the $\overline{\text{P}}$ANDA Detector

Lu Cao

The semileptonic D_s decays are governed by both weak and strong interactions. The strong interaction dynamics can be described by a single form factor $f_+(q^2)$, where q^2 is the invariant mass of the lepton-neutrino system. Theoretical calculations of the form factor offer increasing precision [1]. Therefore, the experimental validation of the results becomes important. I simulate the $\bar{p}p$ interaction to evaluate the detector performance in measuring the semileptonic decay form factor of $D_s^+ \to e^+\nu_e\eta$. With theoretical predictions of the cross section, I obtain a preliminary estimate of the expected count rate for the future data taking at $\overline{\text{P}}$ANDA.

Reconstruction of the decay chain The following decay channels are simulated with 10,000 events at $\sqrt{s} = 4.108$ GeV: $\bar{p}p \to D_s^+D_s^-$; $D_s^- \to K^+K^-\pi^-$; $D_s^+ \to e^+\nu_e\eta$; $\eta \to \pi^+\pi^-\pi^0$; $\pi^0 \to \gamma\gamma$. This simulation is done by using the GEANT4 transport code for the particle tracking through the complete $\overline{\text{P}}$ANDA detector. The related decay models for each channel have been studied in my previous work [2].
To reconstruct D_s^-, I perform the vertex fitting and mass constraint fitting for $(K^+K^-\pi^-)$ combination, where the cut applied on the probability distribution from the χ^2 values is $prob > 0.01$. The reconstruction strategy is slightly complicated for the semileptonic decay chain: $D_s^+ \to e^+\nu_e\eta$, $\eta \to \pi^+\pi^-\pi^0$ and $\pi^0 \to \gamma\gamma$. I started from the combination of two photons detected by the Electromagnetic Calorimeter (EMC). The photon energy threshold is set to be $E_\gamma^{thres} = 20$ MeV to reduce the photon multiplicity caused by bump split off and bremsstrahlung. The mass constraint fitting has been performed on the two-photon system to select the "best" fitted π^0 for reconstructing the mother η. The π^+ and π^- tracks allow the reconstruction of the decay vertex of $\eta \to \pi^+\pi^-\pi^0$. The reconstructed η candidates are selected with a χ^2 probability cut on the mass constraint fit of the three-pion system. After reconstructing the intermediate particles D_s^- and η, the kinematics of the undetected neutrino can be calculated based on a four-momentum condition as

$$M_{\nu_e}^2 = \left(E_{\bar{p}p} - E_{D_s^-} - E_\eta - E_{e^+}\right)^2 - \left|\mathbf{p}_{\bar{p}p} - \mathbf{p}_{D_s^-} - \mathbf{p}_\eta - \mathbf{p}_{e^+}\right|^2,$$

where $E_{\bar{p}p}(\mathbf{p}_{\bar{p}p})$ is the energy (three-momentum) of the initial anti-proton beam and proton target system.

Resolution and count rate With the present software, the decay chain is reconstructed with an efficiency of $\varepsilon(D_s^-) = 17\%$ and $\varepsilon(\eta) = 11\%$. Table 1 summarizes the preliminary results for the reconstruction resolutions for D_s^- and η.

Table 1: Resolutions of reconstructed D_s^- and η candidates.

	σ_{mass}	σ_{vtx} [μm]			σ_{mom} [%]	
	[GeV/c^2]	x	y	z	p_t	p_z
D_s^-	0.0155	67	68	150	3.0	1.4
η	0.0084	287	296	909	2.2	1.7

For the lepton-neutrino system, I reconstruct $\varepsilon(e^+\nu_e) = 2\%$ candidates within the mass window (yellow) of ν_e candidates $\left|M_{\nu_e}^2\right| < 0.1$ GeV^2/c^4 (see Fig.1). Note that the maximum $M^2(e^+\nu_e)$ is consistent with the physical limitation $q^2 \le (M_{D_s} - M_\eta)^2 \approx 2.02$ GeV$^2/c^4$.

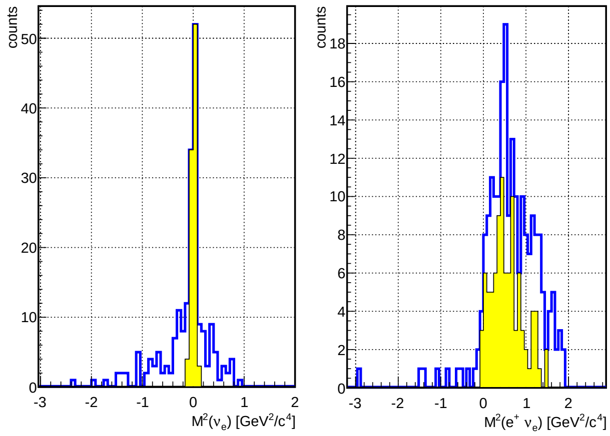

Fig. 1: Left: mass squared of ν_e candidates. Right: invariant mass squared of lepton-neutrino system. The blue line shows the distributions of all candidates; the yellow filed indicates a mass window selection on ν_e, i.e. $\left|M_{\nu_e}^2\right| < 0.1$ GeV^2/c^4.

The theoretical calculations bring a wide range of estimates on the cross section of charm production in proton-antiproton interaction [3, 4]. Assuming the cross section on the production of a D_s pair is 20 nb with a beam momentum of 8.0 GeV/c [4], I estimate the production rate to be approximately 90 events per month for a luminosity of 2×10^{32} cm^{-2}s^{-1} and the average branching ratios $\mathcal{B}(D_s^+ \to \eta e^+\nu_e) = 2.67\%$ and $\mathcal{B}(D_s^- \to K^+K^-\pi^-) = 5.49\%$ [5].

Summary The kinematics of the neutrino have been reconstructed with a complete simulation model of the detector and reconstruction tools. Comparing with the previous results [2], the reconstruction resolution has been improved due to improvements of software in particularly on the kinematic fitter. The count rate of useful events is estimated to be 90 events per month. The upcoming steps will include a modification of the present software to improve the reconstruction efficiency and an investigation of the background channels.

References:

[1] K. Azizi *et al.*, J. Phys. G **38**(9), 095001 (2011); N. Offen *et al.*, Phys. Rev. D **88**(3), 034023 (2013), I. Kanamori, arXiv:1302.6087 [hep-lat].

[2] L. Cao and J. Ritman, J. Phys.: Conf. Ser. **503**(1) 12024 (2014).

[3] A. T. Goritschnig *et al.*, J. Phys.: Conf. Ser. **503**(1) 012012 (2014); A. Khodjamirian *et al.*, Eur. Phys. J. A **48**(3), 31 (2012).

[4] J. Haidenbauer and G. Krein, Phys. Rev. D **89**(11), 114003 (2014).

[5] J. Beringer *et al.*, Phys. Rev. D **86**(1), 010001 (2012).

GPU-based Online Tracking Algorithms for the PANDA Experiment

Andreas Herten, Forschungszentrum Jülich

The $\overline{\text{P}}$ANDA[1] experiment is one of the main experiments at the upcoming FAIR[2] facility, which is currently built in Darmstadt. In the energy region investigated by $\overline{\text{P}}$ANDA, background and signal events have similar signatures. Because of this, a hardware-level triggering mechanism is not foreseen for the experiment. Instead, a fast online event filter substitutes this detector element. The planned event rate for $\overline{\text{P}}$ANDA is $2 \times 10^7/\text{s}$, leading to a raw data rate of approximately $200\,\text{GB}/\text{s}$. For deeper analysis of the physics events offline, event reconstruction in real-time (*online*) has to reduce this data rate by three orders of magnitude, to match the available data storage resources. An important part of the online event reconstruction is particle track reconstruction: From discrete hit points continuous tracks are reconstructed. With this, the particle's momentum can be deduced, giving basis for a subsequent decision by the software trigger to keep or disregard the event.
We investigate the feasibility of using GPUs[3] for online tracking at $\overline{\text{P}}$ANDA. This report introduces basic principles of some of the algorithms considered for GPU online tracking and summarizes the status of the study.

Tracking Algorithms Different types of algorithms are considered for GPU-based track reconstruction in $\overline{\text{P}}$ANDA: Hough Transforms, a Riemann Track Finder, the Triplet Finder. The algorithms have different properties and specialize in distinct features. The algorithms are in varying stages of development with their feature sets being investigated independently.
Two of them are highlighted below.

Triplet Finder An algorithm designed specifically for $\overline{\text{P}}$ANDA's STT[4] is the Triplet Finder. The algorithm centers around the fast generation of center-of-gravity virtual hits (*Triplets*): As a hit is detected in one of a few dedicated STT layers (*pivot layer*), the direct surroundings of the hit is searched for further hits to possibly combine into a Triplet. If two Triplets in two distinct pivot layers are found, they are combined with the interaction point $(0,0)$ to form a track candidate. Benefits of this technique are small computing time, independent computation of the track candidates, and the possibility to obtain particle tracks of sufficient resolution without using the event starting time t_0.
The GPU version of the Triplet Finder is implemented together with the NVIDIA Application Lab. In addition to porting the basic properties and features of the Triplet Finder, multicore-specific optimizations have been made: A *bunching wrapper* packs hits into sets of sizes that best occupy the GPU; GPU-optimized data structures have been implemented (*SoA*[5]); the impact of driver versions, chipset versions, and GPU core clock rates have been studied. The best performance achieved is $14\,\mu\text{s}$ processing time per event. The individual optimizations are described in [1].

Hough Transform An easily parallelizable method to find curves and straight lines connecting points is the Hough Transform (HT). The HT centers around generating a multitude of tracks for a given hit point and filling the parameters, generating the tracks, into a histogram. When repeating this step for all hits of an event, peaks will form in the histogram. The peaks are equivalent to the parameters describing the tracks connecting all the hit points best. The method is based on work by [2] and [3] and has been described in previous versions of this report, e.g. [4].
A newly-developed HT involves the generation of circles (**Circle Hough**, CH). The CH algorithm takes a hit point, either an isonchronous STT hit, or any other hit of a tracking detector (MVD, GEM), and connects it to the interaction point. Continuing, it samples possible circles through the two fix points by generating circle center points. The three points (the currently investigated hit point, $(0,0)$, the sampled circle center) describe a circle as a candidate for a particle's track. The circle centers are sampled to curvatures equivalent to the highest possible value of transverse momentum in $\overline{\text{P}}$ANDA, $p_t = 15\,\text{GeV}/c$. A circle is generated by the equation

$$(x_C, y_C)_{ij} = (x_i + s_{ij}\cos\varphi_j, y_i + s_{ij}\sin\varphi_j), \tag{1}$$

$$s_{ij} = \frac{\rho_i^2 - x_i^2 - y_i^2}{x_i\cos\varphi_j + y_i\sin\varphi_j + \rho_i}, \tag{2}$$

for a investigated hit point with coordinates (x_i, y_i) and possible ischrone radius ρ_i. The sampling of circle centers is done with steps of the angle φ_j in the range of $\varphi_j \in [0°, 360°]$. The circle centers, (x_C, y_C), of each sampled circle of each investigated hit point is filled into a two-dimensional histogram. After processing all hits, the coordinates of the center of a circle describing a track going through the hit points best emerges as the bin with the highest multiplicity.
The CH is able to reconstruct $\geq 75\,\%$ of the tracks in a benchmarking channel involving the reconstruction of the daughter particles of the process $\bar{\text{p}}\text{p} \to \text{D}^+\text{D}^- \to \text{K}^-\pi^+\pi^+\text{K}^+\pi^-\pi^-$, studied at $6.5\,\text{GeV}/c$ beam momentum. The parameters of the CH algorithms are currently being investigated and optimized. A first implementation of the core of the CH is implemented on the GPU using CUDA. The circle centers, generated by means of Equation 1, are computed in parallel for a given hit point. Figure 1 shows the dependence of the computing time needed to generate 360 circles for a hit point on the GPU thread size, a quantity specifying the number of concurrently invoked GPU processes. A NVIDIA GTX 580 GPU is compared with a Intel Core i5 CPU. In this first implementation, a speed-up of factor 20 is reached. First studies show that this number can be further increased when expanding the parallelism beyond a single hit to a set of hits, leveraging more GPU parallel processing power.

Summary and Outlook Different track reconstruction algorithms have been successfully implemented on GPUs. The latest one, the Circle Hough algorithm, shows promising results in terms of computing performance and reconstruction

[1] Anti-Proton Annihilation at Darmstadt
[2] Facility for Antiproton and Ion Research
[3] Graphics Processing Units
[4] Straw Tube Tracker
[5] A structure of arrays, SoA, combines arrays of different variables into a `struct` / `class`. The data of each variable array lies then contiguous in one piece in the memory, quickening access for the appropriate parallel algorithm.

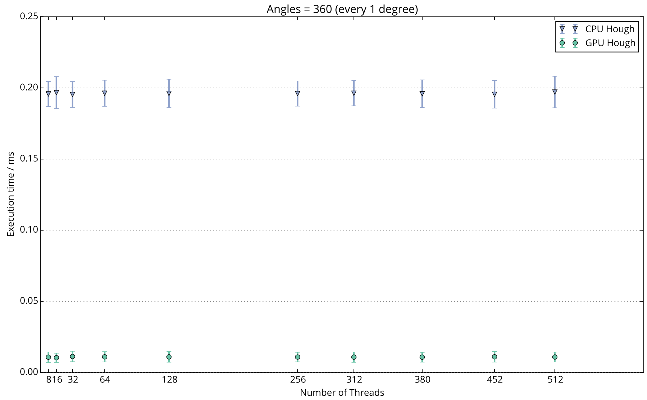

Fig. 1: Circle Hough algorithm execution times. Compared is generation of circle center coordinates on GPU (green points) to generation on CPU (purple triangles). The GPU is a NVIDIA GTX 580, the CPU an Intel Core i5 (3.3 GHz).

efficiency. Both quantities are subject to current research and will further improve in the future.

References:

[1] A. Adinetz, A. Herten, J. Kraus, M. C. Mertens, D. Pleiter, T. Stockmanns, P. Wintz, *Triplet Finder: On the Way to Triggerless Online Reconstruction with GPUs for the PANDA Experiment*, Procedia Computer Science, Vol. 29(0) pp. 113 – 123, (2014)

[2] P. Hough, Machine Analysis of Bubble Chamber Pictures, Proc. Int. Conf. High Energy Accelerators and Instrumentation, 1959.

[3] R. O. Duda & P. E. Hart, Use of the Hough Transformation to Detect Lines and Curves in Pictures, Comm. ACM, Vol. 15, pp. 11 – 15 (January, 1972).

[4] A. Herten, GPU-based Online Tracking Algorithms for the PANDA Experiment, Annual Report 2013.

FEE-free signal processing system for the PANDA Straw Tube Tracker

S. Costanza [1], A. Erven [2], W. Erven [2], T. Hahnraths - von der Gracht [2], L. Jokhovets [2], P. Kulessa [2,3], B. Lorentz [2],

R. Nellen [2], H. Ohm [2], D. Prasuhn [2], K. Pysz [2,3], J. Ritman [2], V. Serdyuk [2], P. Wintz [2], P. Wuestner [2]

The architecture of the Front-End Electronics (FEE) free readout system for the Straw Tube Tracker (STT) of the PANDA experiment has been defined. The experience gained from the operation of the central straw tracker of WASA at COSY played an important role in the development of the STT readout. The results of the laboratory tests as well as the tests performed with the use of the COSY beam proved that the active elements of the signal processing electronics can be located back-end from the STT detector. Fig. 1 presents the concept of the proposed STT signal processing scheme.

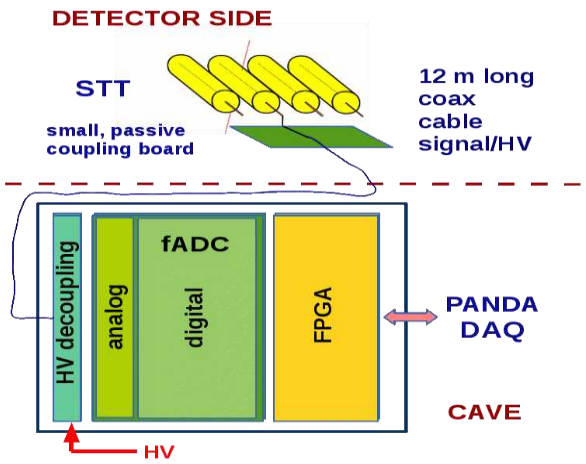

Fig. 1. Proposed architecture of the signal-processing chain in the FEE-free readout system of the PANDA STT.

The signals generated in the individual straw tubes are transferred from the detector to the electronic racks located in the HESR cave in vicinity of the PANDA apparatus via 12 m long coaxial cables with 1.1 mm diameter. These cables are coupled directly to the upstream end of the straw tubes using only small and passive PCB boards. Amplification and shaping happens at the far end of the coaxial cables in amplifiers with low-noise input stages. They will be integrated into the flash-ADC (fADC) board. The input connector in front of the amplifier will contain passive components for decoupling of the analog signals from the detector high voltage. The fADC will be followed by a dedicated FPGA housed in an ATCA crate. Here signals are analysed in terms of the particle's passage time and energy loss. In addition, some pre-analysis and selection of events is foreseen. The data will be transferred to the PANDA DAQ-system.

The advantages of the FEE-free readout for the PANDA-STT are as follows:

- only a minimum space at the upstream end region of the STT detector is required,
- the material budget in this region is reduced,
- no heat is generated front-end at the detector,
- no additional cables for high-voltage supply to the detector are needed,
- no radiation damage of electronics front-end at the detector,
- the active elements of the readout electronics are completely accessible from outside,
- single failure channels in the STT can be decoupled individually from the high voltage.

The FEE-free readout was optimized with respect to critical aspects: Over two weeks the very thin coaxial signal cables were subject to voltages far beyond the straw operating voltage of about 1800 V. Leakage currents were found to be less than 0.1 nA for voltages below 3500 V. Mechanical stress did not affect this finding. A prototype of the low-noise amplifier was developed and the whole chain from the straws to the remotely placed amplifier crate has been prepared for in-beam tests. The effect of the cable capacitance on the thermal noise level of the amplifier which acts as a load of approx. 1.2 nF was found to be tolerable. From the measured rms noise voltage and the rise time of the straw signals a contribution to the time resolution of 100 ps was estimated. Assuming a linear space-time relationship this corresponds to about 3 μm which can be considered negligible in comparison with the expected overall spatial resolution of about 150 μm. Additional noise from electromagnetic interference was kept under a negligible level with proper shielding and grounding of all critical components. The whole straw detector including the cables were wrapped with 12 μm Mylar foil having 50 nm Al on either side. The conductive material, properly connected to all components, guaranteed equal ground potential for detector and amplifiers.

The digital part of the readout system comprising the fADC and the FPGA board is under development in the ZEA-2 Institute of Forschungszentrum Juelich [1].

The performance test of the FFE-free readout system with the use of the proton beam from COSY accelerator has been performed in December 2014. The test setup is presented in Fig. 2. 128 straw tubes similar to the PANDA-STT straw type were arranged in 8 close-packed layers and illuminated with the direct proton beam. Signals from the straw tubes were transferred to the external amplifier via 12 m long coaxial HV cables. The construction and parameters of the signal preamplifier located at the far end of the coaxial cable were the same as the analog input stage of the future fADC board.

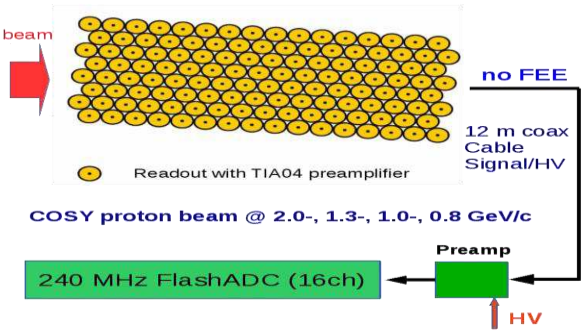

Fig. 2. Description of the setup for December 2014 test with the COSY beam.

Instead of the planned fADC-FPGA system which is currently under development the 240 MHz flash-ADC of the WASA at COSY type was used to sample the STT signals. The pulse analysis was performed offline. The beam momenta were selected in order to examine the detector and the readout system performance for minimum ionizing particles as well as for those of higher energy losses.

The appropriate tracking procedure and the energy loss (dE/dx) estimation have been used in order to determine the spatial and the energy resolution of the detector and signal processing system. Both the distributions of the tracking residuals as well as the truncated energy loss spectra have narrow Gaussian shapes as shown in examples in Fig. 3 and Fig. 4, respectively. A truncation of 20% of the hits per track with highest dE/dx was applied.

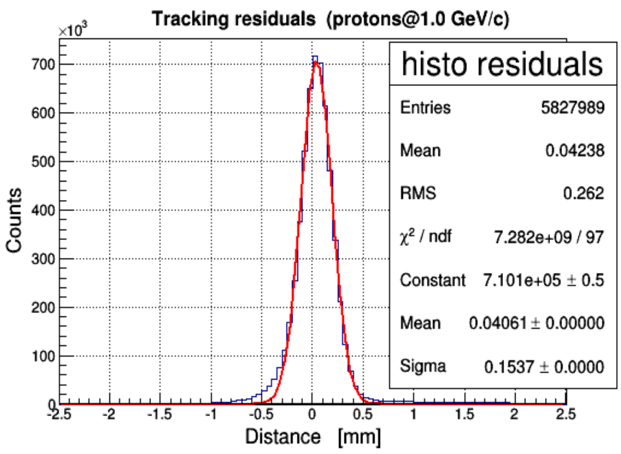

Fig. 3. Residual distribution of reconstructed tracks for the 1.0 GeV/c proton momentum.

Table 1 summarises the results obtained during the December 2014 beam test of the FFE-free readout system of the PANDA-STT. Results of tests with cosmic rays are included as well.

Both the position resolution as well the energy resolution of the tested system fulfill the requirements defined for the PANDA-STT in the Technical Design Report [2].

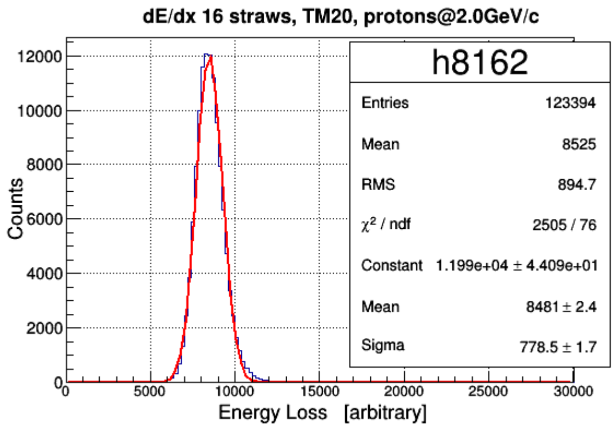

Fig. 4. Truncated-mean energy loss distribution for 2.0 GeV/c protons.

Beam momentum / cosmic ray	Spatial resolution [μm]	Energy resolution [%]
2.0 GeV/c	160 ±10	9.2 ±1.0
1.3 GeV/c	157 ±10	9.1 ±1.0
1.0 GeV/c	154 ±10	9.0 ±1.0
Cosmic rays	154 ±10	-

Table 1. The spatial and the energy resolution obtained for the PANDA STT prototype and the FEE-free readout system in the December 2014 test with the COSY proton beam. The spatial resolution for a measurement of cosmic rays is also listed.

[1] "*Investigation of an ADC based signal processing and design of an ATCA data acquisition system unit for the Straw Tube Tracker at PANDA*", L. Jokhovets et al., DOI: 10.1109/NSSMIC.2013.6829734

[2] "*Technical design report for the PANDA (AntiProton Annihilations at Darmstadt) Straw Tube Tracker*", PANDA Collaboration (W. Erni et al.). 2013. 104 pp., Eur.Phys.J. A49 (2013) 25, DOI: 10.1140/epja/i2013-13025-8, e-Print: arXiv:1205.5441

[1] INFN Pavia, [2] FZ Juelich, [3] IFJ PAN Kraków

This work was partially supported by the FFE program of ICHP-FZJ.

Test Beam with a $\overline{\text{P}}$ANDA Trapezoidal Prototype Sensor

Dariusch Deermann

The innermost subdetector of $\overline{\text{P}}$ANDA will be the Micro Vertex Detector (MVD) which uses both silicon pixel and strip sensors. It's purpose is to measure precise points of particle tracks in order to enable secondary vertex reconstruction with a resolution in the 0.1 mm range.

It has four barrel layers around the beam axis with the inner two consisting of pixel sensors and the outer two of strip sensors. Furthermore, six discs are placed in the forward direction. Each of those discs has a center part with pixel sensors. The outer two also have a double ring structure around the pixel disc, with each ring carrying 24 trapezoidal strip sensors.

In January, a test beam for the $\overline{\text{P}}$ANDA MVD's trapezoidal prototype sensors was held at COSY. The prototype has 512 strips with a pitch of 67.5 µm per sensor side, while the final version will have the same external geometry but consist of 768 strips with a pitch of 45 µm. The strips are aligned parallel to the long edges and have a stereo angle of $15°$ between p- and n-side strips. The sensors bulk material is n^--doped with p^+-doped strips on the p-side and n^+-doped strips on the n-side.

A picture of the sensor placed in a readout board can be seen in Figure 1. The readout is done by four APV25 ASICs [1] per sensor side.

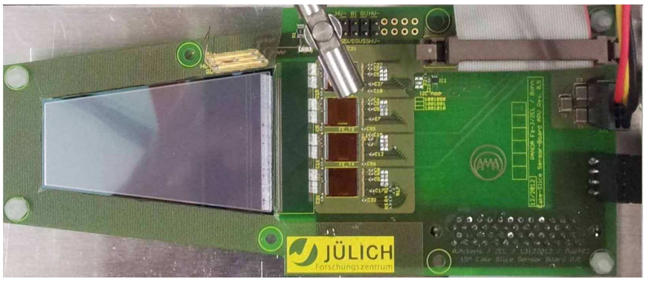

Fig. 1: Sensor with readout board.

The APV25 is a triggered readout chip with 128 channels. The triggers were generated by a coincidence signal of four scintillators that were placed in the beam. More information about the DAQ can be found in [2].

The test beam was a proton beam with a momentum of 0.8 GeV/c and an intensity of ~ 20 kHz. The DAQ reached a trigger rate of ~ 600 Hz.

Figure 2 shows the correlation between the p- and n-side energy loss per cluster. Since a real hit deposits the same amount of charge on the p- and n-side, the entries along the diagonal are coming from real hits. The p-side showed more noise than the n-side which can be seen by the densely populated band close to the Y-axis with low energy deposition in the p-side clusters. The corresponding but less populated band close to the X-axis represents noise entries from the n-side. There are also some entries with high energy depositions on both sensor sides which are quite distant from the diagonal peak. Those entries are *ghost hits*, which means that two or more hits were present at the same time. In that case, when the hits deposited different amounts of charge, wrong combinations of p- and n-side clusters will appear at a distance to the diagonal according to their energy difference.

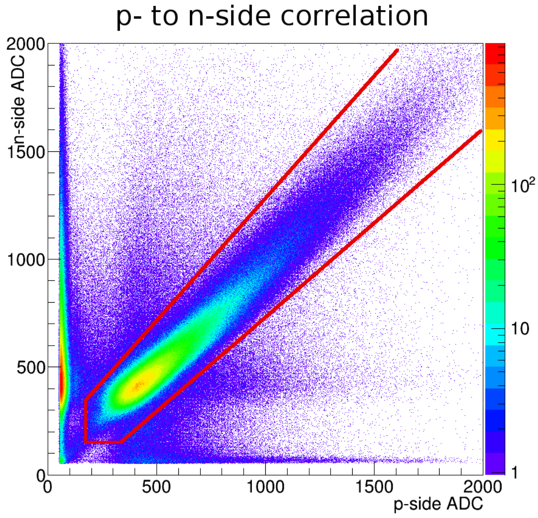

Fig. 2: Correlation between p- and n-side cluster energy deposition. The red line indicates the selected region.

The red line in the figure indicates the cut position that was chosen to discriminate noise and ghost entries.

For k simultaneous hits, k^2 possible combinations of their p- and n-side clusters exist. Therefore, if all clusters were found and no additional noise clusters were created, the number of ghost hits could be calculated as $k^2 - k$. But due to efficiency and noise, the number of clusters on p- and n-side are not always identical so that the number of ghost hits has to be approximated by:

$$k_\mathrm{p} \cdot k_\mathrm{n} - \sqrt{k_\mathrm{p} \cdot k_\mathrm{n}} \tag{1}$$

From a total of 56617 ghost hits, 21398 could not be suppressed by the correlation cut, which gives a suppression success rate of 62%.

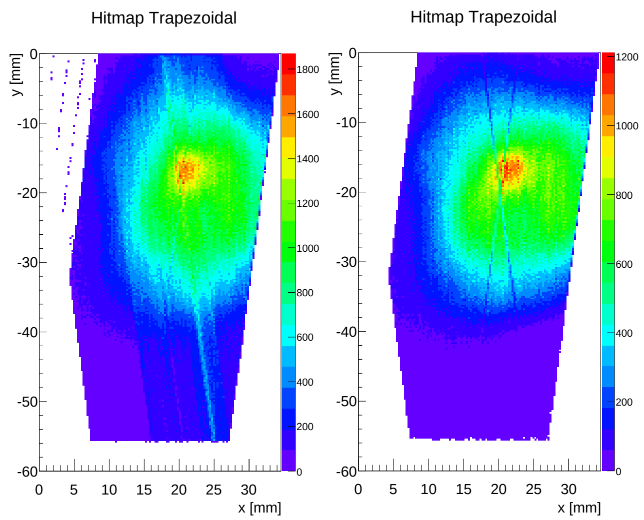

Fig. 3: Hitmap of the sensor. without cuts (left), with cuts (right)

Figure 3 shows a comparision of the resulting hitmap before and after selecting the data as described above. Without the cuts some structures parallel to the left sensor edge dominate parts of the hitmap. These are mainly the noise entries from the p-strips which are aligned in that direction. The upper left corner of the sensor is missing in the hitmap as the corresponding APV25 chip for that part of the n-side was broken. The spatial resolution for clusters with two strip signals can be improved by using the η *method*. Here, η is defined as:

$$\eta = \frac{q_r}{q_r + q_l} \tag{2}$$

And the hit position can be calculated as:

$$x(\eta') = x_l + \frac{\int_0^{\eta'} \frac{\mathrm{d}N(\eta)}{\mathrm{d}\eta}\mathrm{d}\eta}{N_0} \tag{3}$$

Here, x_l is the center of the left strip of the two strip cluster, $N(\eta)$ is the η distribution and N_0 the total number of entries in the η distribution. In order to use this method the η distribution must be measured. This has been done for the prototype during the test beam separately for different cluster energies and the result can be seen in Figure 4.

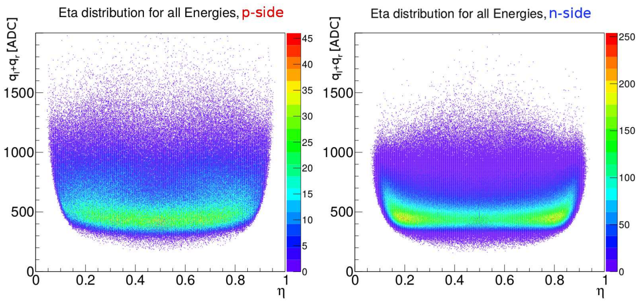

Fig. 4: η distribution for the p- and n-side.

The first test beam with a $\overline{\text{P}}$ANDA trapezoidal prototype sensor was successful and showed that the majority of noise and ghost hits can be discriminated by a p- to n-side correlation cut. At the $\overline{\text{P}}$ANDA experiment, the remaining ghost hits may be rejected by tracking algorithms which include the track information from the hole detector setup.
Furthermore, the η distribution was determined to increase the spatial resolution of two strip clusters.

References

[1] L.L. Jones *et al.* “The APV25 Deep Submicron Readout Chip for CMS Detectors”. In: *Proc. 5th Conf. Electronics for LHC Experiments* (1999), pp. 162–166.

[2] M. Becker *et al.* “FPGA-based readout for double-sided silicon strip detectors”. In: *Journal of Instrumentation* 6.01 (2011), p. C01008. URL: http://stacks.iop.org/1748-0221/6/i=01/a=C01008.

Data Analysis of the KOALA Experiment Commissioning at COSY

Qiang Hu[1,2], Huagen Xu[2], James Ritman[2]

The KOALA experiment is dedicated to measure antiproton-proton elastic scattering in a large range of squared 4-momentum transfer t (0.0008 - 0.1 GeV^2) at HESR. The KOALA experiment will determine the elastic differential parameters (σ_T, ρ and b). The elastically scattered antiproton and recoil proton will be measured by tracking detectors in the forward angle region and by recoil detectors near θ=90°, respectively.

The recoil detectors consist of two silicon detectors and two germanium detectors which cover a polar angle range from 71° to 91.5°. The silicon and germanium detectors are single-sided structure with 1.2 mm pitch on the front side. The two silicon detectors (Si_#1 and Si_#2) have the same sensitive area 76.8 mm (length) × 50 mm (width) × 1 mm (thickness). The two germanium detectors (Ge_#1 and Ge_#2) have the same active area 80.4 mm (length) × 50 mm (width), but with thickness of 5 mm and 11 mm, respectively. The silicon detectors will detect recoil protons with energy up to 12 MeV and the germanium detectors will measure recoil protons with energy from 12 MeV to 60 MeV.

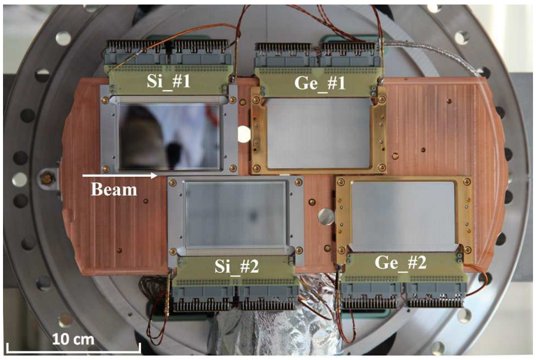

Fig. 1: Photo of recoil detectors for pp elastic scattering experiments at COSY.

One recoil arm has been built and commissioned at COSY. The detector layout of the commissioning experiment is shown in Fig. 1. Data of proton-proton elastic scattering has been taken at several beam momenta. The energy spectra of all strips on silicon and germanium detectors at P_{lab} = 3.2 GeV/c are shown in Fig. 2 after clustering. The candidate elastic events clearly form a band on the silicon and germanium detectors. The elastic events on Ge_#1 and Ge_#2 can be separated completely from the background. However, the events on Si_#1 and Si_#2 are mixed with background when the recoil proton's energy is less than ∼ 600 keV. Fig. 3 shows the single energy spectra at different recoil angles. It is shown that the elastic peak sits on top of the background and moves away with increasing the recoil angle. The recoil peak can be distinguished from the background when $90° - \theta = \alpha > 2.82°$. In the small recoil angle region ($\alpha < 2.82°$), the background is stable in neighboring strips with a Landau shape. Therefore, it is reasonable to subtract the background from the single energy spectrum with a Landau distribution to get the elastic scattering counts in each strip.

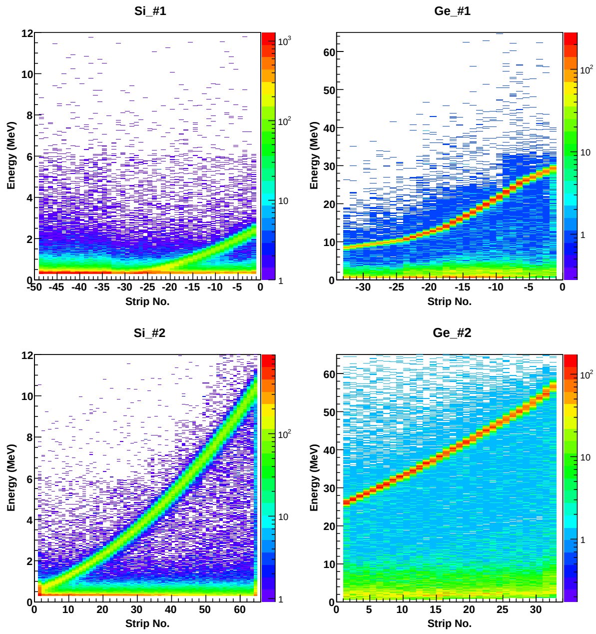

Fig. 2: Energy spectra after clustering. The scattering angle α increases from left to right.

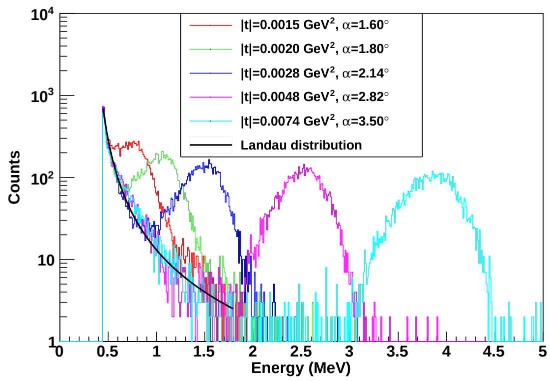

Fig. 3: Energy spectra of individual strips at different recoil angles.

After subtracting the background, the centroid energy of the recoil peak as well as the elastic scattering yield were obtained. Based on the centroid energy and the yield, the $|t|$ ($|t| = 2m_pT_p$) distribution has been reconstructed after acceptance correction. The differential counts as a function of $|t|$ is shown in Fig. 4. To determine the elastic scattering differential parameters, one typical method is to analysis the characteristic shape of the $|t|$-spectrum with the parameterized expressions 1-4[1] and 5.

$$\frac{d\sigma}{dt} = \frac{\pi}{k^2}\left|f_c^{i\delta} + f_n\right|^2 = \frac{d\sigma_c}{dt} - \frac{d\sigma_{int}}{dt} + \frac{d\sigma_n}{dt}, \quad (1)$$

$$\frac{d\sigma_c}{dt} = \frac{4\pi\alpha^2 G^4(t)(\hbar c)^2}{\beta^2 t^2}, \quad (2)$$

$$\frac{d\sigma_{int}}{dt} = \frac{\alpha\sigma_{tot}G^2(t)}{\beta|t|}e^{-\frac{1}{2}b|t|}(\rho\cos\delta + \sin\delta), \quad (3)$$

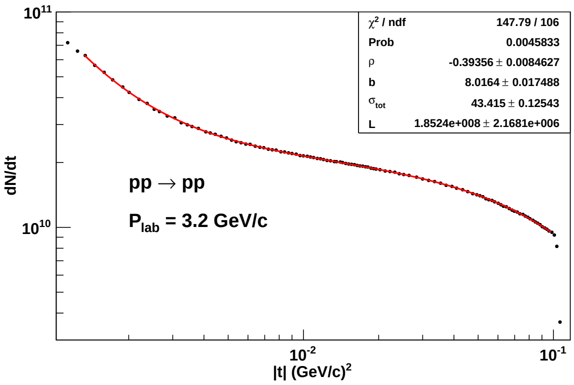

Fig. 4: $|t|$ distribution at $P_{lab} = 3.2$ GeV/c.

$$\frac{d\sigma_n}{dt} = \frac{\sigma_{tot}^2(1+\rho^2)e^{-b|t|}}{16\pi(\hbar c)^2}, \tag{4}$$

where $\frac{d\sigma_c}{dt}$ is coulomb term, $\frac{d\sigma_{int}}{dt}$ is nuclear-coulomb interference term and $\frac{d\sigma_n}{dt}$ is nuclear term. α is the fine-structure constant ($\alpha \simeq 1/137$), $G(t)$ is proton form factor and δ is phase factor.

$$\frac{dN}{dt} = L \cdot \frac{d\sigma}{dt}. \tag{5}$$

where L is the integrated luminosity to be determined.

By fitting the $|t|$-spectrum in the range of $[0.00125, 0.1]$ (GeV/c)^2, the elastic scattering differential parameters and integrated luminosity L are determined as shown in Fig. 4. The values of $\sigma_{tot} = 43.42 \pm 0.13(sta.)$ mb, $\rho = -0.3936 \pm 0.0085(sta.)$, $b = 8.016 \pm 0.017(sta.)$ (GeV/c)$^{-2}$ and $L = 1.852 \times 10^8 \pm 2.168 \times 10^6$ cm^{-2} are obtained at $P_{lab} = 3.2$ GeV/c. The statistical errors of σ_{tot} and b are smaller than 1% except for $\sim 2.15\%$ of ρ and $\sim 1.17\%$ of L. These fitting errors are consisting with the results of simulation which is based on ideal detector setting. From simulation, the systematic errors of σ_{tot}, ρ and b are 0.02%, 1.06% and 0.06%, respectively. Taking into account all of the contribution of the parameters, the integrated luminosity with precision $< 3\%$ could be achieved.

[1]Institute of Modern Physics, CAS, 730000 Lanzhou, China

[2]Forschungszentrum Juelich, 52425, Germany

[1] M. M. Block *High-energy $p\bar{p}$ and pp forward elastic scattering and total cross sections.* Rev. Mod. Phys, 1985, 57(2):563.

Search for polarization effects in the antiproton production process

D. Grzonka for the P349 collaboration

While polarized proton beams and targets are routinely prepared, the possibilities for the preparation of a polarized antiproton beam are still under discussion. Summaries of the various possibilities can be found in [1], [2], [3]. Most of the methods are not usable due to the extremely low expected numbers of polarized antiprotons or the low degree of polarization and for some methods reasonable calculations are not possible since relevant parameters are not known. The most simple possibility for a polarized antiproton beam may be the production process itself if the antiproton production process creates some polarization. It is well known that particles, like e.g. Λ-hyperons, produced in collisions of high energy unpolarized protons show a significant degree of polarization. Maybe also antiprotons are produced with some polarization but up to now no experimental studies have been done in this direction. Therefore an experiment for the study of possible polarization of produced antiprotons has been performed at CERN.

The antiprotons were produced by the 24 GeV/c proton beam of the CERN/PS accelerator resulting in an antiproton momentum distribution centered around 3.5 GeV/c. The experiment was placed at the T11 beam line at a production angle of about 150 mrad with an acceptance of $\pm$ 3 mrad horizontally and $\pm$ 10 mrad vertically. The beam line was adjusted to a momentum of 3.5 GeV/c for negatively charged particles. About $5 \cdot 10^5$ particles/spill were delivered with a spill length of about 400 ms. The detector arrangement for the measurement is shown in Fig. 1. It consists of scintillators

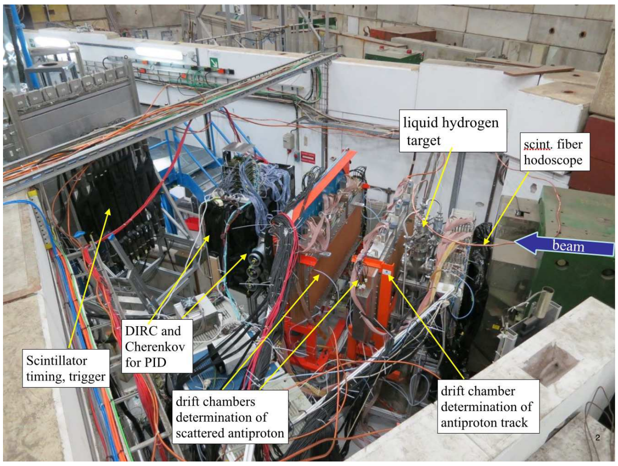

Fig. 1: The detector arrangement at the T11 beam line. The beam is entering from the right and hits start scintillator, beam hodoscope, first drift chamber, scattering target, drift chamber pair, Cherenkov detector, DIRC, and scintillator hodoscope.

for trigger signal generation and beam profile measurements, a drift chamber stack to measure the track of the produced antiproton, an analyzer target, a second drift chamber set to reconstruct the track of a scattered antiproton, a Cherenkov detector for pion discrimination, a DIRC for offline particle identification, and another scintillator hodoscope for trigger and $\bar{p}/\pi^-$ distinction by time of flight. At the exit of the beam line tube which ends in front of the last beam line dipole a scintillation detector was mounted which was used as a start detector for the timing and trigger generation. A scintillation fibre hodoscope followed to determine the beam profile. The drift chambers used for these studies were the COSY-11 chambers with track resolutions in the order of 1 mrad. As analyzer target a liquid hydrogen cell with a length of 15 cm was used. At the exit of the tracking system, an aerogel Cherenkov detector (n $\sim$ 1.03) to discriminate the expected high pion background was installed. Behind the Cherenkov counter a DIRC with Plexiglas as radiator was mounted for offline particle identification.

The Cherenkov veto signal reduced the trigger rate by a factor of about 10 which allowed to accept more or less all triggered events by the data acquisition system based on TRB boards from GSI. In the preliminary offline analysis the antiprotons could be very well separated from pions (separation $\sim 2.6\ \sigma$) by the signals from the DIRC as demonstrated in Fig. 2 which shows the positions of the maxima of the reconstructed arcs of the Cherekov ring. A much better separation is expected in the final analysis, in test measurements at COSY with 3.5 GeV/c protons a p/π separation of 7.8 σ was achieved.

The determination of the polarization will be performed for events in the Coulomb-Nuclear interference (CNI) region corresponding to an antiproton scattering angle around 20 mrad where the analyzing power is rather well known. The data are presently under analysis and a second measurement will be performed in 2015 to increase the statistics to a level which allows to determine the polarization (P) to a precision of P $\pm$ 0.05.

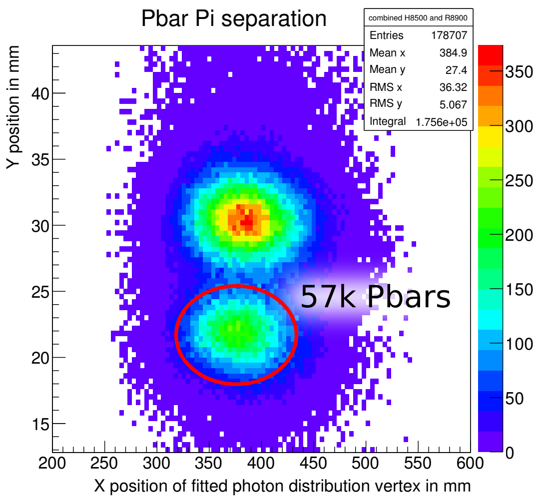

Fig. 2: Positions of the Cherenkov arcs maxima reconstructed from the measured photon distribution. The antiprotons at lower y-values which are proportional to the Cherenkov angles are marked by the red ring.

References:

[1] A. D. Krisch, *AIP Conf. Proc.* **145** (1986)

[2] E. Steffens, *AIP Conf.Proc.* **1008**, 1-5 (2008), *AIP Conf.Proc.* **1149**, 80-89 (2009)

[3] H. O. Meyer, *AIP Conf.Proc.* **1008**, 124-131 (2008)

Measurement of the analysing power in $\vec{p}d$ elastic scattering at small angles*

Z. Bagdasarian[a,b], S. Dymov[a], A. Kacharava[a], G. Macharashvili[b,c],
D. Mchedlishvili[a,b], N. Lomidze[a,b] and M. Tabidze[a,b] for the ANKE collaboration

The ANKE collaboration has performed the experiment using a transversely polarised proton beam incident on an unpolarised hydrogen or deuterium cluster jet target [1]. Six beam energies of $T_p = 0.796$, 1.6, 1.8, 1.965, 2.157 and 2.368 GeV were used. Even though the main goal of the experiment was to study *pp* and *pn* scattering spin observables, it was also possible to extract the analysing power for pd elastic scattering. This report will summarise the preliminary results of the *pd* analysing power at the aforementioned energies in the scattering range from 4 to 28 degrees in the center-of-mass.

The scattered deuterons were detected at the ANKE spectrometer using the Silicon Tracking Telescopes (STT). The two STTs were placed inside the vacuum chamber, to the left and right of the beam close to the unpolarised deuterium cluster target. Each STT consists of three layers of double-sided silicon strip detectors. These layers of 70 μm, 300 μm, and 5000 μm thickness were placed 2.8, 4.6 and 6.2 *cm* away from the target, covering laboratory angles $75^\circ < \theta_{lab} < 140^\circ$.

In order to calculate the analysing power, we had to measure the polarisation of the beam and the asymmetry of the scattered deuterons. Cycles of 180 s or 300 s duration were used, with the last 20 s being reserved for the measurement of the beam polarisation with the EDDA detector. The 7μm diameter carbon fibre target was moved in the beam at the end of the every cycle. The polarimeter consists of 29 pairs of half-rings, and thanks to the known effective analysing powers of the rings, it was possible to measure the polarisation via every ring. The weighted averages over time and polar angle were taken as the final values of the polarisation. The systematic uncertainty of the polarisation measurement was estimated to be 3% [2] and it dominates the uncertainty of the final *pd* analysing power.

The elastic deuterons were registered in the STTs, measuring the total kinetic energy as well as polar angle. However, greater precision is achieved in the angle of the stopped particles by deducing it from the energy measured in the telescope rather than from a direct angular measurement [3]. The elastic deuterons were identified through the missing mass evaluation in the $pd \to dX$ reaction. The clear proton peak is seen when one deuteron is detected in the STT (Fig. 1).

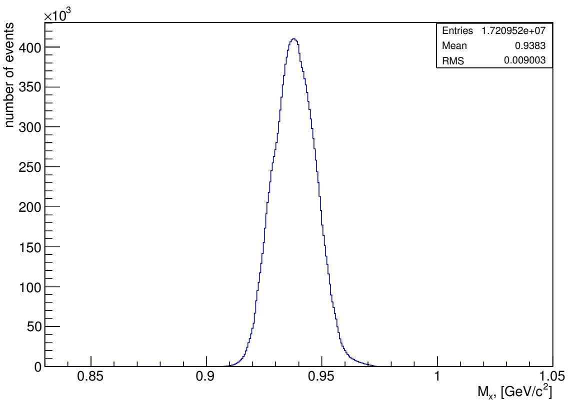

Fig. 1: Missing mass spectra obtained for $pd \to dX$ at the beam energy T_p=1.8 GeV.

The so-called cross-ratio method [4] allows one to eliminate first-order systematic errors, for that reason the polarisation of the beam was reversed every successive cycle.

Forming the geometrical means of the yields to the left $L = \sqrt{L_1 L_2}$ and to the right $R = \sqrt{R_1 R_2}$ with respect to the beam polarisation direction, the asymmetry is calculated as

$$\varepsilon(\theta) = \frac{L(\theta) - R(\theta)}{L(\theta) + R(\theta)} \tag{1}$$

in each θ scattering angle interval. Finally, the analysing power A_y is calculated as

$$A_y(\theta) = \frac{\varepsilon(\theta)}{P\langle cos\phi\rangle} \tag{2}$$

In our geometry $\langle cos\phi\rangle \approx 0.966$, where ϕ is the azimuthal angle.

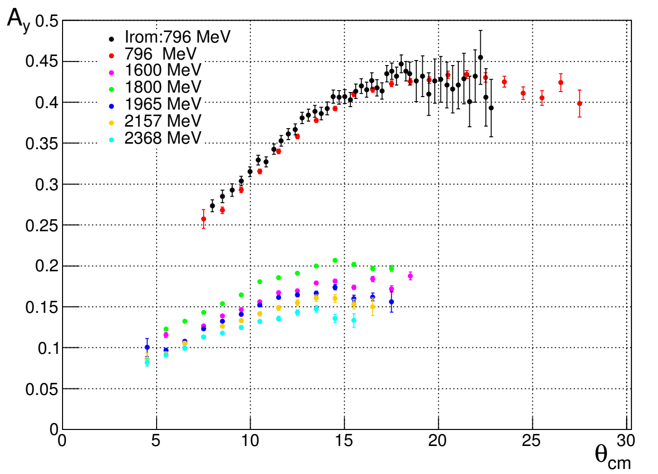

Fig. 2: *pd* elastic scattering analysing power A_y (preliminary) results, along with the existing experimental data from SATURN at 796 MeV [5]. ANKE results include statistical errors only

The results of the measurements of A_y at all six energies are shown on the Fig. 2. Our measurements at 796 MeV agree with SATURN measurements [5] within the systematic error bars. The results at five other energies can be used for the polarimetry at various polarised experiments, as well as could be useful input for the model calculations [6].

References:

[1] Z. Bagdasarian et al, *COSY Proposal* #212, 2012.
[2] E. Weise, *EDDA internal report* #00=01, 2000
[3] G. Macharashvili, *Technical report* #24, 2013
[4] G.G. Ohlsen and P.W. Keaton, *Nuclear Instruments and Methods* 109(8):41-59, 1973
[5] F. Irom et al. *Phys. Rev. C* 28: 2380-2385, 1983
[6] A. Temerbayev, Yu. Uzikov. *Physics of Atomic Nuclei* 78(1) 35-42, 2015

[a] IKP FZJ, Jülich, Germany
[b] HEPI TSU, Tbilisi, Georgia
[c] LNP JINR, Dubna, Russia

* supported by Shota Rustaveli National Science Foundation of the Republic of Georgia

Identification of the quasi-free reaction $\mathbf{p + d \to d + \eta + p_{sp}}$ *

D. Schröer†, C. Fritzsch, D. Guderian, A. Khoukaz, M. Mielke, M. Papenbrock for the ANKE-Collaboration

In order to further investigate the η-nucleus final state interaction (FSI) and the question on η-mesic nuclei the reaction $p + d \to d + \eta + p_{sp}$ was measured at the ANKE spectrometer. The deuteron acts in this case as an effective neutron target with the proton being a spectator particle. By using two different beam momenta, $p_{beam} = 2.09$ GeV/c and $p_{beam} = 2.25$ GeV/c, the Fermi motion inside the target allows to extract total and differential cross sections in a region from threshold up to an excess energy of Q=100 MeV.
The cross section can be written as

$$\frac{d\sigma}{d\Omega} = \frac{p_f}{p_i} \cdot |f(\vartheta)|^2 \qquad (1)$$

with p_f and p_i being the cnter of mass final/initial state momentum and f the production amplitude. Assuming there are no higher partial waves than s-wave, this amplitude can be separated in a constant term f_{prod} and a term describing the final state interaction between deuteron and η meson

$$\text{FSI} = \frac{1}{1 - iap_f} \qquad (2)$$

with the complex scattering length a [1]. To pin down the range in which this ansatz is valid the onset of higher partial waves has to be identified. Therefore differential cross sections will be determined to resolve the first deviation from a flat scattering angle distribution in cosϑ.

To achieve all of this precise measurement and identification of the deuteron and the spectator proton has to be ensured.
The proton is detected in one of two Silicon Tracking Telescopes (“STT”) [2]. One STT, consisting of three layers of silicon, is placed at each side of the target in a distance of 2.8 cm.

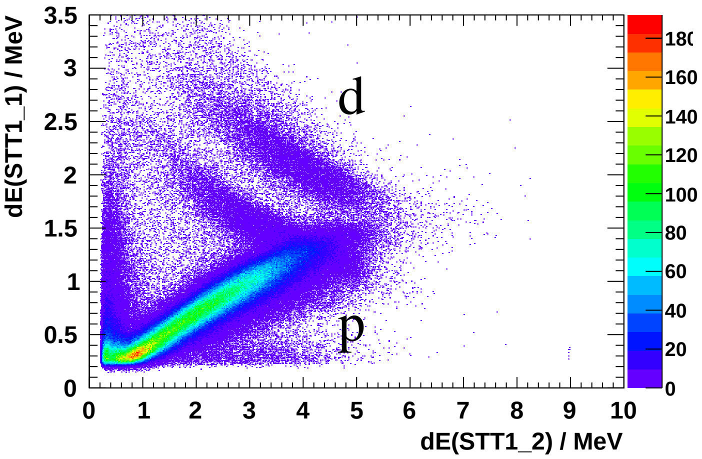

Fig. 1: Energy loss in the first layer as a function of the energy loss in the second layer in one of the two STTs for one run. Well separated proton and deuteron bands can be seen.

Here one hit is demanded in the first two STT layers. This request results in an energy range for the spectator particles from 2.5 MeV up to 8 MeV which assures that observed protons originate only from spectator reactions. The separation of protons and deuterons, mainly from elastic scattering, is obtained by comparing the energy losses in the first to layers, where clean deuteron and proton bands are visible (Fig. 1).

The identification of the deuterons is more challenging due to a huge proton background. It is detected in the ANKE Forward System (“Fd system“) and selected via the energy loss information in the scintillator hodoscopes. As the energy loss of deuterons and protons is very similar in this momentum region the determination of cut values is demanding.
For this reason a special trigger was used during the beam time slecting events with a particle in the Fd system and a pion in the positive system. By applying cuts on the Time-of-Flight difference between the pions and the particle in the Fd system the proton background can be suppressed, so that the deuteron band becomes visible.This technique allows a precise determination of energy loss cuts for the deuteron.

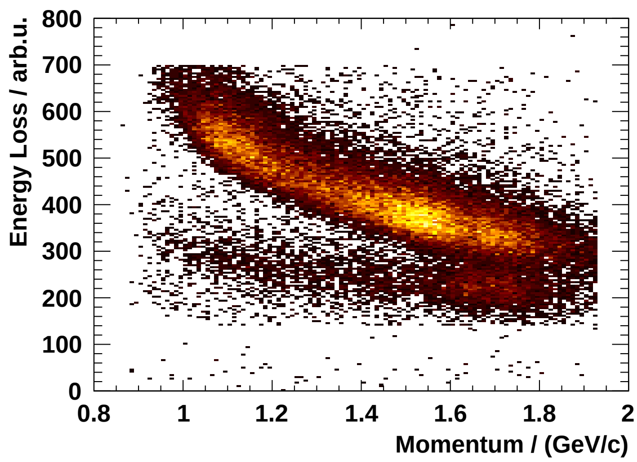

Fig. 2: Energy loss versus momentum in the Fd system after applying ToF cuts on the reaction $p + d \to d + \pi^+ + n_{sp}$. The deuterons (upper band) are clearly visible while the protons (lower band) are suppressed.

With both particles, proton and deuteron, the reaction $p + d \to d + \eta + p_{sp}$ can be identified via the missing mass and first results on the cross section will be available soon.

References:

[1] C. Wilkin et al., Phys. Lett. B 654, 92-96, 2007
[2] A. Mussgiller, Identification and Tracking of Low Energie Spectator Protons, doctoral thesis, Universität Köln, Germany,2007
[3] M. Rump, bachelor thesis, Westfälische Wilhelms-Universität Münster, Germany, 2013

*Supported by COSY-FFE
†Institut für Kernphysik, Westfälische Wilhelms-Universität, 48149 Münster, Germany

Luminosity determination via dp-elastic scattering at ANKE *

C. Fritzsch †, D. Guderian, A. Khoukaz, M. Mielke, M. Papenbrock, and D. Schröer for the ANKE-Collaboration

The ANKE collaboration has performed a beam time to determine the η meson mass with high precision using the $d + p \rightarrow {}^3\text{He} + \eta$ reaction [1] and to study the two pion production using $d + p \rightarrow {}^3\text{He} + \pi^+ + \pi^-$ [2]. In order to determine the η mass, data has been studied at 18 deuteron beam momenta in a range between $3120.17\ \text{MeV}/c \leq p_d \leq 3204.16\ \text{MeV}/c$ which could be extracted very accurately via the resonant depolarisation technique with a precision of $\Delta p_d/p_d < 6 \times 10^{-5}$ [1, 3]. Moreover, due to the high statistics of more than 1×10^5 ${}^3\text{He}\eta$ events per energy in combination with full angle coverage these high precision ANKE data allow to investigate the total and differential cross sections of the reaction $d + p \rightarrow {}^3\text{He} + \eta$. Such data are of special interest since they differ strongly from a pure phase space behaviour near threshold which is explained by an unexpected strong final state interaction (FSI) between η mesons and ^{3}He nuclei which could lead to the formation of a quasi bound state of the $\eta{}^3$He-system [4, 5]. To extract total and differential cross section values a careful luminosity determination was performed for each of the 18 beam momenta of the beam time via dp-elastic scattering. Because of the broad data base of available differential cross sections in the range of $-t \approx 0.1\ (\text{GeV}/c)^2$ the dp-elastic scattering is very well suited as normalization reaction. The identifcation of the reaction was ensured via the missing mass technique (cf. figure 1) by detecting deuterons in the forward system which carry a momentum close to the beam momentum due to a low momentum transfer on the target proton.

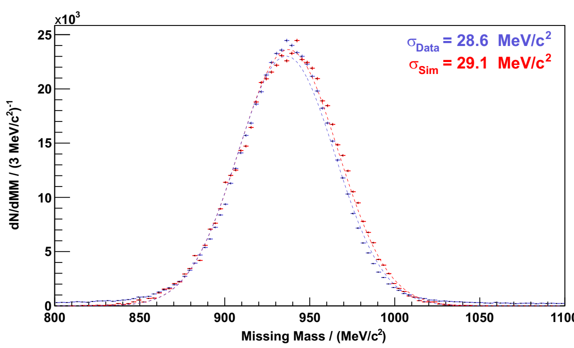

Fig. 1: Missing-mass distribution of the identified deuteron (blue) compared with the corresponding Monte Carlo simulation (red).

In this way luminosities could be extracted with high precision ($\Delta_{stat} = 1\%$, $\Delta_{sys} = 6\%$). Especially the systematic uncertainties were improved by at least a factor of two compared to previous determinations. At higher momentum transfers ($-t \geq 0.12\ (\text{GeV}/c)^2$) the reference data show only a limited number of data points and discrepancies between data sets (cf. figure 2).

Due to the high quality and statistics of the ANKE data set on the dp-elastic scattering in this momentum transfer region, new precision data can be provided. For this purpose and to verify the results of the dp-elastic scattering an independent

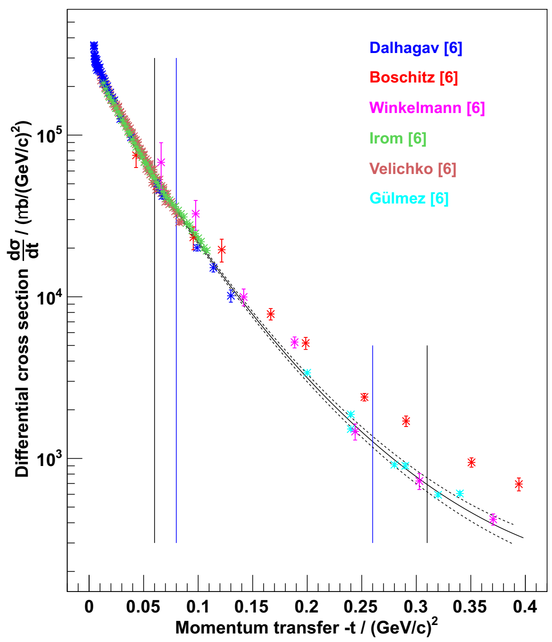

Fig. 2: Reference cross sections for dp-elastic scattering as a function of momentum transfer $-t$. The black vertical lines tag the range of ANKE acceptance and the blue vertical lines the range which was used for the luminosity determination.

absolute normalization via $d+p \rightarrow d+\pi^0+p_{sp}$ is currently in progress. The identifcation of the dp pairs in the forward detection system of the ANKE spectrometer is ensured via the time-of-flight difference between the particles. Result will be available soon, so that it will be possible to determine precise total and differential cross sections for the η production up to an excess energy of $Q = 15$ MeV as well as differential cross sections for the dp-elastic scattering in the interesting momentum transfer region of $0.08\ (\text{GeV}/c)^2 \leq -t \leq 0.26\ (\text{GeV}/c)^2$. The final η production data will be discussed together with results from a further beam time from WASA-at-COSY investigating the behaviour at excess energies of $13\ \text{MeV} < Q < 81\ \text{MeV}$ [7].

References:

[1] P. Goslawski *et al.*, Phys. Rev.D **85**, 112011 (2012).
[2] M. Mielke *et al.*, Eur. Phys. J. A **50**, 102 (2014).
[3] P. Goslawski *et al.*, Phys. Rev. ST-AB **13**, 022803 (2010).
[4] T. Mersmann *et al.*, Phys. Rev. Lett. **98**, 242301 (2007).
[5] C. Wilkin *et al.*, Phys. Lett. B **654**, 92 (2007).
[6] V. Dalhagav *et al.*, Yad. Fiz. **8**, 342 (1968);
E. T. Boschitz *et al.*, Phys. Rev. C **6**, 457 (1972);
E. Winkelmann *et al.*, Phys. Rev. C **21**, 2535 (1980);
F. Irom *et al.*, Phys. Rev. C **28**, 2380 (1983);
G. N. Velichko *et al.*, Yad. Fiz. **47**, 1185 (1988);
E. Gülmez *et al.*, Phys. Rev. C **43**, 2067 (1991).
[7] N. Hüsken, FZ Jülich annual report, (2014).

*Supported by COSY-FFE
†Institut für Kernphysik, WWU Münster, Germany

Measurements of the $\vec{p}n$ quasi-free elastic scattering at ANKE*

S. Barsov[1], Z. Bagdasarian[2,4], D. Chiladze[3], S. Dymov[3], A. Kacharava[2], G. Macharashvili[3], S. Merzlyakov[2], S. Mikirtychyants[1,2], R. Schleichert[2], S. Trusov[2] for the ANKE collaboration.

As discussed in [1], the nucleon-nucleon interaction amplitudes extracted by the phase-shift analysis are of general importance for study of any hadronic process at intermediate energies. The significant contribution to a small angle domain of the *np* elastic scattering has been done at ANKE during last years by measuring the interaction of deuteron beam with the hydrogen target [2]. However, in this case the beam energy is limited by 1.15 GeV/nucleon. To approach the higher energy domain, where data are very scarce, measurements were performed at ANKE using the polarized proton beam and unpolarized deuterium cluster target.

The data have been taken at 6 proton beam energies of 0.8, 1.6, 1.8, 2.0, 2.2 and 2.4 GeV. The orientation of beam polarization along Y-axis was changing every 3 minutes. The value of polarization was measured by the EDDA polarimeter. Two Silicon Tracking Telescopes were installed at 3cm distance to the left and the right from the deuterium target to detect low energetic particles in coincidence with fast particles going into the ANKE Forward detector (Fd). The missing mass technique and the asymmetric Fd acceptance were exploited for identification of the quasi-free *NN* elastic scattering as described in [3]. It must be noted that other data on the *pd* [4] and quasi-free *NN* elastic scattering [5], which can be used for comparison with our results, exist at $T_p =$ 0.8 GeV only.

Under the given experimental conditions, one has to derive polarization observable from the simple asymmetry of counts corresponding to different orientations of the beam polarization. Such asymmetry is very sensitive to the relative normalization of counts measured, in fact, at different luminosity and different beam polarization values. Taking into account the significant discrepancy between the analyzing power for the quasi-free $\vec{p}n$ elastic scattering obtained at ANKE and the $A_y^n(\Theta_{cm})$ from [5], which was mentioned in our previous report [3], a new normalization procedure was developed. It was verified by the $\vec{p}d$ elastic scattering. The angular dependence of asymmetry well coincides with the angular dependence of the analyzing power $A_y(\Theta_{cm})$ measured in [4]. (Fig. 1) Furthermore, the average beam polarization value determined from the asymmetry is of **0.501+/-0.001(stat)** which is in a good agreement with the polarization measured by the EDDA polarimeter (**0.4890+/-0.0003(stat)+/-0.015(sys)**) as well as with our previous value (**0.513+/-0.001(stat)**).

However, the $A_y^n(\Theta_{cm})$ derived from the same set of data was still found to be about 30% smaller than the analyzing power published in [5] (Fig. 2, left panel). As follows from Fig. 2 (the right panel), the observed discrepancy seems to be related to different ways of the *pn* elastic scattering identification used in these two experiments. The quasi-free scenario is generally assumed to be realized when the momentum transfer from a beam particle to a scattered one (P_t) is large enough as compared with the "spectator" particle momentum (P_{sp}). In contrast to [5] where both scattered particles (proton and neutron) were detected, at ANKE we have detected the "spectator" proton in coincidence with the scattered proton. Since in our case the "spectator" proton momentum can only be reconstructed when $P_{sp} > 70 MeV/c$, the $P_{sp}/P_t > 0.3$ at the 0.8 GeV beam energy. Nevertheless, the fact that at $P_{sp}/P_t < 0.4$ the $A_y^n(\Theta_{cm})$ measured at ANKE gets close to the expected value gives a good basis for the further analysis of data taken at higher beam energies.

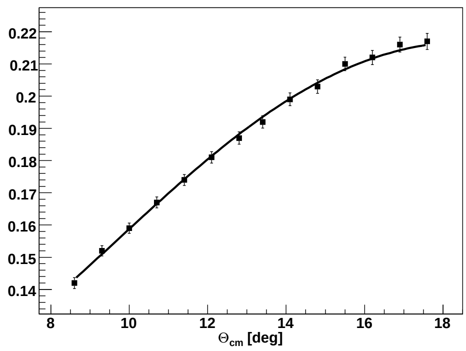

Fig. 1: The $\vec{p}d$ elastic scattering asymmetry (points) versus Θ_{cm} angle is shown together with the $A_y(\Theta_{cm})$ from [4] (line) scaled with the only parameter equal to the average beam polarization at $T_p = 0.8$ GeV.

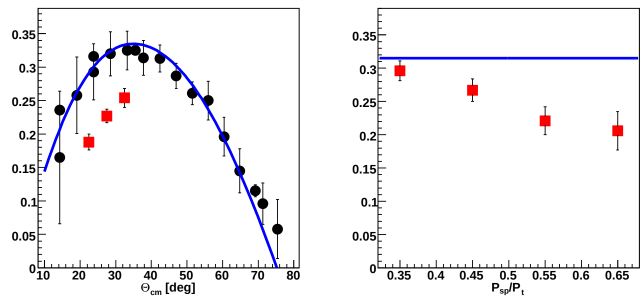

Fig. 2: The quasi-free $\vec{p}n$ elastic scattering at $T_p = 0.8$ GeV. **Left panel** represents the $A_y^n(\Theta_{cm})$ from [5] (black points) versus Θ_{cm} angle. Red squares show the $A_y^n(\Theta_{cm})$ measured at ANKE. In this case data are averaged over full available P_{sp}/P_t range. The current SAID solution is shown by the solid line.
Right panel demonstrates the A_y^n measured at ANKE within the $\Theta_{cm} = 25° - 30°$ angular range as a function of the P_{sp}/P_t ratio. Here, the solid line indicates the $A_y^n(\Theta_{cm} = 27.5°)$ predicted by SAID.

References:

[1] Proposal COSY-212 (2012)
[2] D.Mchedishvili, PhD thesis (2013)
[3] S.Barsov et al., IKP Annual Rep. (2013)
[4] F.Irom et al., Phys.Rev. C 28, 2380 (1983)
[5] M.L.Barlett et al., Phys.Rev. C 27, 682 (1983)

1 PNPI, 188350 Gatchina, Russia
2 IKP, FZ Jülich, 52425 Jülich, Germany
3 JINR, 141980 Dubna, Russia
4 HEPI TSU, 0186 Tbilisi, Georgia

* supported by COSY-FFE

Investigation of Dipion Final State Interactions in $pp \to pp\eta[\eta \to \pi^+\pi^-\gamma]$ with WASA-at-COSY

Daniel Lersch for the WASA-at-COSY collaboration

The decay $\eta \to \pi^+\pi^-\gamma$ is suitable to study the chiral anomalies of QCD [1, 2]. The decay amplitude is solely determined by the box anomaly in the chiral limit [1, 2, 3]. However, when going to physical masses, the triangle anomaly dominates the box anomaly because of final state interactions between the two pions. Thus, a correct description of this decay can only be achieved by including final state interactions [3, 4, 5, 6]. The experimental observables to test interaction models are the relative branching ratio: $\frac{\Gamma(\eta\to\pi^+\pi^-\gamma)}{\Gamma(\eta\to\pi^+\pi^-\pi^0)}$ and the photon energy E_γ distribution [7, 8, 9].

In order to measure both quantities in one experiment, the reaction $pp \to pp\eta[\eta \to \pi^+\pi^-\gamma]$ has been investigated. The data have been acquired during 2008, 2010 and 2012 using the WASA-at-COSY facility [10].

Competing processes to the η production are multi-pion production reactions such as $pp \to pp\pi^+\pi^-\pi^0$ and $pp \to pp\pi^+\pi^-$ which dominate the signal reaction $\eta \to \pi^+\pi^-\gamma$. In order to reduce these background contributions a kinematic fit as well as the rejection of low energetic satellite clusters in the calorimeter have been implemented in the recent analysis.

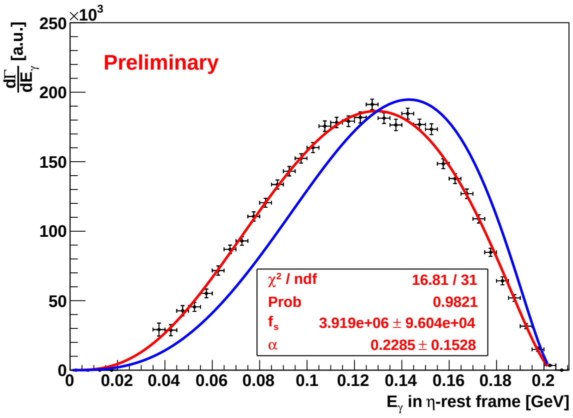

Fig. 1: Single photon energy distribution (black symbols) E_γ obtained from the analysis of $\sim 42\%$ of the $pp \to pp\eta$ 2010 data set.

Fig. 1 shows the single photon energy distribution (black symbols) of $\eta \to \pi^+\pi^-\gamma$ after the analysis steps discussed above. The blue curve corresponds to a photon energy distribution assuming no final state interaction bewteen the two pions. The red curve is related to a model independent approach using a single parameter α to describe the shape of the E_γ distribution and therefore contributions from final state interactions. The description of the pion-pion interactions is done by using the pion vector form factor, which is independent of the underlying decay mechanism [6], modified by a factor $(1+\alpha s_{\pi\pi})$ [6] such that any decay specific interaction process is related to $\alpha \neq 0$.

Including studies of systematic effects related to the data analysis, the final results for the decay observables of $\eta \to \pi^+\pi^-\gamma$ are given by:

$$\frac{\Gamma(\eta\to\pi^+\pi^-\gamma)}{\Gamma(\eta\to\pi^+\pi^-\pi^0)} = 0.197 \pm 0.001_{stat} \pm 0.02_{sys} \qquad (1)$$

and:

$$\alpha = (0.229 \pm 0.153_{stat} \pm 0.269_{sys} \pm 0.02_{theor})\,\mathrm{GeV}^{-2} \qquad (2)$$

Both results are in agreement with theoretical models including Vector Meson Dominance to describe the dipion final state interactions [3, 4]. Eq. 1 is also in agreement with the recent PDG value [11]. In a next step, the remaining $pp \to pp\eta$ data will be analysed.

References:

[1] J. Wess and B. Zumino. Consequences of anomalous ward identities. *Physics Letters*, **B37**, 95, 1971

[2] E. Witten. Global aspects of current algebra. *Nuclear Physics*, **B223**,422-432, 1983

[3] B. R. Holstein, Allowed Eta-Decay Modes and Chrial Symmetry, *Phys. Scripta*, **T99**, 55-67, 2002

[4] M. Benayoun et al. Anomalous η/η' Decays: The Triangle and Box Anomalies. *European Physics Journal*, **C31**, 525-547, 2003

[5] J. Bijnens et al. Three-Pseudoscalar Photon Interactions in Chiral Pertubation Theory. *Physics Letters*, **B37**, 488-494, 1990

[6] F. Stollenwerk et al. Model independent approach to $\eta \to \pi^+\pi^-\gamma$ and $\eta' \to \pi^+\pi^-\gamma$. *Physics Letters*, **B707**, 184-190, 2012

[7] The CLEO collaboration. Measurement of prominent η branching fractions. *Physics Review Letters*, 99(122001), 2007

[8] The KLOE collaboration. $\Gamma(\eta \to \pi^+\pi^-\gamma)/\Gamma(\eta \to \pi^+\pi^-\pi^0)$ with the KLOE detector. *Physics Letters*, **B718**, 910-914, 2013

[9] The WASA-at-COSY collaboration. Exclusive Measurement of the $\eta \to \pi^+\pi^-\gamma$ Deacy. *Physics Letters*, **B707**, 243-249, 2012

[10] H.-H Adam et al., Proposal for the wide angle shower apparatus WASA-at-COSY, (2004)

[11] K. A. Olive et al. (Particle Data Group). Review of Particle Physics. *Chinese Physics*, **C38**, 2014

Charge symmetry breaking in the dd $\longrightarrow$ ^{4}Heπ^0 reaction with the WASA-at-COSY experiment

Maria Żurek

Probing elementary symmetries and symmetry breaking tests our understanding of Quantum Chromodynamic (QCD). Isospin symmetry, which is an approximate symmetry under every rotation in isospin space, has two known sources of violation, namely the electromagnetic interactions and the up-down quark mass difference [1, 2]. Studies of reactions in which these two sources can be disentangled allows access to quarks mass ratios [1, 3].

For the energies available at COSY (COoler SYnchrotron) QCD cannot be treated perturbatively. Instead, particle interactions can be described by means of Chiral Perturbation Theory (χ_{PT}). On the hadronic level, the isospin breaking observables are dominated by the pion mass difference ($\Delta\pi$), which is an almost purely electromagnetic effect. This makes it difficult to get access to the term linked to the quark mass difference. However, for a special case of isospin symmetry breaking, namely charge symmetry breaking, the $\Delta\pi$ term does not contribute. Charge symmetry is a rotation of 180° angle in isospin space, which exchanges up and down quarks.

One of the key projects of the WASA-at-COSY experiment is the investigation of the charge symmetry breaking reaction dd $\longrightarrow$ ^{4}Heπ^0 at $Q = 60$ MeV. The goal is to provide further experimental input for χ_{PT} calculations of the proton-neutron mass difference caused by the up and down quark mass difference, especially the contribution of higher partial waves. In a first experiment, the total cross section of the dd $\longrightarrow$ ^{4}Heπ^0 reaction at $Q = 60$ MeV has already been obtained [4]. However, for decisive results on higher partial waves, higher statistics and increased sensitivity are needed. Therefore, an 8 week long experimental run dedicated to the dd $\longrightarrow$ ^{4}Heπ^0 reaction at beam momentum of $p_d = 1.2$ GeV/c was performed in spring 2014.

The Forward Detector of WASA was modified by removing most of the layers of the plastic scintillator detectors. This allowed the measurement of the time-of-flight (ToF) of the outgoing ^{4}He. Feasibility studies showed that the ^{4}He -^{3}He separation is significantly improved in comparison to the previous measurement by introducing particle identification based on ToF.

Calibration of time-of-flight and energy losses were performed. For the ToF calibration, the registered time information of the outgoing ^{3}He from the two-body dd $\longrightarrow$ ^{3}Hen reaction was used. First the alignment of the time readouts from every element of the first two scintillator detectors — the Forward Window Counters — was obtained. Then, the time of flight values from data were shifted to the values obtained from Monte Carlo simulations of the dd $\longrightarrow$ ^{3}Hen reaction. In addition, a correction of the dependence on the azimuthal angle was applied for every element of the Forward Window Counters.

The subsequent calibration of energy losses in the Forward Window Counters is based on ToF. It was performed by comparing the data to a simulated sample of ^{3}He in the Forward Detector. The dependency between the energy losses dE_{MC} in the Forward Window Counters and ToF (dE_{MC}(ToF)) for ^{3}He was obtained from Monte Carlo simulations as a function of the azimuthal angle. For data, the dependency between ToF and the uncalibrated energy losses dE_{data} was extracted (ToF(dE_{data})). Linking these two dependencies, a function to recalculate the energy losses in ADC channels to energy losses in GeV was obtained. Furthermore, a run-dependent correction was applied, to address a varying gain of the detector elements.

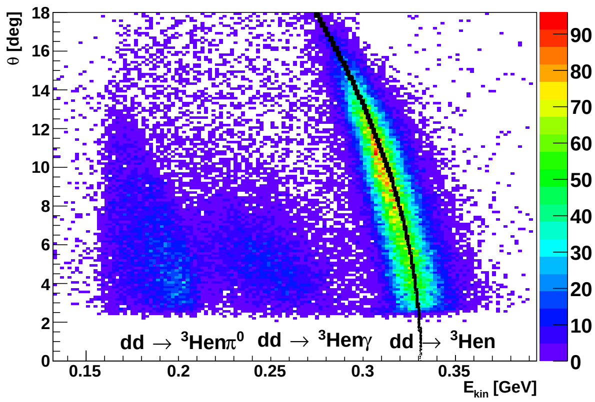

Fig. 1: The kinetic energy E_{kin} versus the azimuthal angle θ of ^{3}He in the Forward Detector. Black line: the kinematics of the two-body dd $\longrightarrow$ ^{3}Hen reaction.

For the full kinematic information of the outgoing particles in the Forward Detector — apart from the azimuthal and vertical angle from the Forward Proportional Chambers — the kinetic energy E_{kin} is needed. The reconstruction procedure is based on the dependency between E_{kin} and ToF or dE in the Forward Window Counters. It was determined as a function of the azimuthal angle and separately for ^{4}He and ^{3}He. Fig. 1 shows the dependency between the azimuthal angle and the reconstructed E_{kin} for ^{3}He in the Forward Detector. The regions of the dd $\longrightarrow$ ^{3}Henπ^0, dd $\longrightarrow$ ^{3}He$\gamma\pi^0$, and dd $\longrightarrow$ ^{3}Hen reactions are indicated.

In a next step, a kinematic fit will be introduced and a cut on the cumulative probability distribution will be applied for the dd $\longrightarrow$ ^{3}Henπ^0 background subtraction. In addition, the energy loss information from the last plastic scintillator layer of the Forward Detector, which is not yet included, will improve the ^{4}He -^{3}He separation. With a clean dd $\longrightarrow$ ^{4}Heπ^0 signal sample, the total and differential cross section will be extracted.

References:

[1] J. Gasser, H. Leutwyler, Phys. Rept. 87 (1982) 77.
[2] S. Weinberg, Trans. N.Y. Acad. Sci. 38 (1977) 185.
[3] G. A. Miller, B. M. Nefkens, I. Šlaus., Phys. Rept. (1990), 194.
[4] P. Adlarson et al. (WASA-at-COSY Collaboration), Phys. Lett. B 739 (2014) 4449.

Investigation of total cross section structures in the pd → ^{3}Heη reaction with WASA-at-COSY*

N. Hüsken†, F. Bergmann†, K. Demmich†, A. Khoukaz†, and K. Sitterberg†

The production cross section of the pd → ^{3}Heη reaction has been studied in great detail in the near threshold region [1, 2, 3, 4, 5], whereas at higher excess energies the amount of available data is limited [6, 7, 8, 9]. Moreover, while the data from ANKE and WASA/PROMICE expose a total cross section plateau away from threshold, recent results from the WASA-at-COSY experiment [10] suggest an unexpected narrow variation of the total cross section at $Q = 48.8\,\mathrm{MeV}$ as shown in Figure 1.

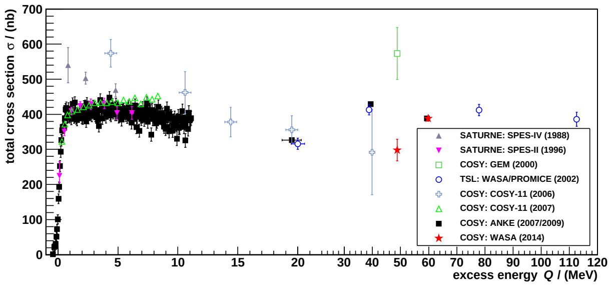

Figure 1: Total cross section data for the reaction pd → ^{3}Heη obtained by [1] - [10] as a function of the excess energy Q. Figure taken from [10].

The WASA-at-COSY experiment is perfectly suited to study the energy dependence of both the total and differential cross sections of the pd → ^{3}Heη reaction. Therefore, a beam time was realized in May 2014 in order to investigate the excess energy region of interest. The COSY storage ring has provided protons with 15 different beam momenta between $p_p = 1.60\,\mathrm{GeV/c}$ and $p_p = 1.74\,\mathrm{GeV/c}$ resulting in a Q-value range between $Q \approx 13.6\,\mathrm{MeV}$ and $Q \approx 80.9\,\mathrm{MeV}$ with a step size of about 4.8 MeV.

In order to identify the pd → ^{3}Heη reaction, the missing mass technique is used. A careful energy loss calibration of the WASA Forward Detector is currently being performed, so that the full four-momenta of the ^{3}He nuclei can be reconstructed precisely by measuring the deposited energy as well as both the azimuthal and polar scattering angles ϕ and ϑ. Preliminary missing mass spectra for ^{3}He nuclei stopped in two different layers of the Forward Range Hodoscope (FRH) are shown in figure 2 for a beam momentum of $p_p = 1.70\,\mathrm{GeV/c}$. Clear signals of both the pd → ^{3}Heη and the pd → ^{3}Heπ^0 reaction can be obtained on top of a sizable background resulting from multi-pion production. First estimations yield more than 120000 reconstructed pd → ^{3}Heη events for each beam momentum.

The ongoing analysis will result in both differential and total cross sections for all 15 beam momenta with the high statistics obtained for each excess energy providing an estimated point-to-point uncertainty of the order of 8 % (not including an overall normalization uncertainty). In order to extra total cross sections, an absolute normalization will be done using the pd → ^{3}Heπ^0 reaction.

This new data set will allow us to study possible cross section variations in great detail. Furthermore, precise total and differential cross sections will be provided, which are of high interest for the understanding of the underlying production processes and therefore the development of theoretical production models [11].

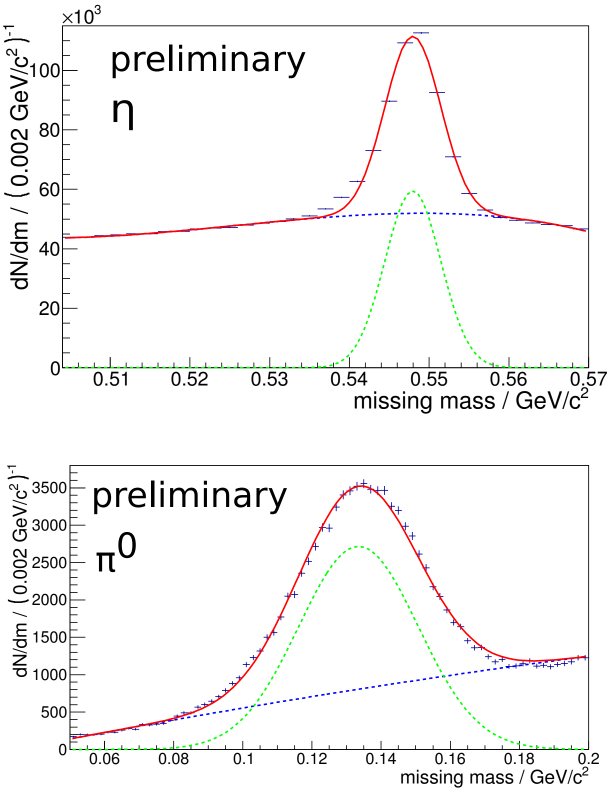

Figure 2: Preliminary missing mass plots for ^{3}He nuclei stopped in layer one (top) and layer two of the Forward Range Hodoscope (bottom). A combined fit (shown in red) of a polynomial and a gaussian is used to describe the data. The doted blue and green lines show only the polynomial or the gaussian respectively.

References

[1] T. Mersmann *et al.*, Phys. Rev. Lett. **98**, 242301 (2007).
[2] J. Smyrski *et al.*, Phys. Lett. B **649**, 258 (2007).
[3] J. Berger *et al.*, Phys. Rev. Lett. **61**, 919 (1988).
[4] B. Mayer *et al.*, Phys. Rev. C **53**, 2068 (1996).
[5] H.-H. Adam *et al.*, Phys. Rev. C **75**, 014004 (2007).
[6] T. Rausmann *et al.*, Phys. Rev. C **80**, 017001 (2009).
[7] R. Bilger *et al.*, Phys. Rev. C **65**, 044608 (2002).
[8] R. Bilger *et al.*, Phys. Rev. C **69**, 014003 (2004).
[9] M. Betigeri *et al.*, Phys. Lett. B **472**, 267 (2000).
[10] P. Adlarson *et al.*, Eur. Phys. J. A **50:**, 100(2014).
[11] B. K. Jain, private communication.

*Supported by COSY-FFE and the European Union Seventh Framework Programme (FP7/2007-2013) under grant agreement n 283286

†Institut für Kernphysik Westfälische Wilhelms-Universität, 48149 Münster, Germany

Search for C-violation in the Decay $\eta \to \pi^0 + e^+ + e^-$ at WASA-at-COSY*

F. Bergmann†, K. Demmich†, N. Hüsken†, K. Sitterberg†, A. Täschner†, and A. Khoukaz†

One main emphasis of the WASA-at-COSY experiment is the analysis of rare and forbidden η-decays. One focus is the search for C-violation in the decay $\eta \to \pi^0 e^+ e^-$. The dominant C conserving contribution to this decay is $\eta \to \pi^0\gamma^*\gamma^* \to \pi^0 e^+ e^-$, which is suppressed by a factor of approximately 10^{-8} Compared to the decay $\eta \to \pi^0\gamma\gamma$ [1]. The decay $\eta \to \pi^0\gamma^* \to \pi^0 e^+ e^-$ is forbidden since it violates the C-parity conservation. Hence, an observation of the decay $\eta \to \pi^0 e^+ e^-$ with a branching ratio well above 10^{-12} would be an indication for the presence of C-violation. The current upper limit of the branching ratio is $4 \cdot 10^{-5}$ [2].

In order to search for the C-violating decay $\eta \to \pi^0\gamma^* \to \pi^0 e^+ e^-$ a careful description of this decay in Monte Carlo simulations is required. As the on-shell decay $\eta \to \pi^0\gamma$ not only violates the C-parity but also the angular momentum conservation, the decay model has been modified in Monte Carlo accordingly. Fig. 1 shows the invariant mass distribution of the e^+e^- pair for this decay model (green dashed line). Further possible decay models assume a decay via a dark boson. Simulations for such a decay have been performed as well. An invariant mass distribution assuming a dark boson mass of $140\ \mathrm{MeV}/c^2$ (width: $100\ \mathrm{keV}/c^2$) is shown in blue (solid line).

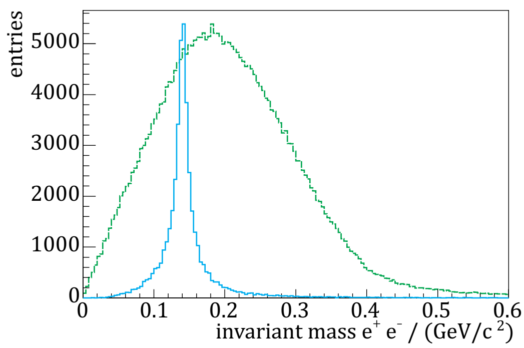

Figure 1: Monte Carlo simulation: invariant mass of the e^+e^- pair for the simulated reaction $\eta \to \pi^0\gamma^* \to \pi^0 e^+ e^-$ (green dashed line) and for the simulated reaction $\eta \to \pi^0 X \to \pi^0 e^+ e^-$ with a dark boson mass of $140\ \mathrm{MeV}/c^2$ (blue solid line).

For the analysis data sets of two η production reactions are used, namely $\mathrm{pd} \to {}^3\mathrm{He}\eta$ and $\mathrm{pp} \to \mathrm{pp}\eta$ from the years 2008 to 2012. While for the first one about $3 \cdot 10^7$ such η-events are on tape, about $5 \cdot 10^8$ $\mathrm{pp} \to \mathrm{pp}\eta$ events have been recorded. Since the ratio of η-events to background from direct (multi-)pion production is higher for the ^{3}He data the analysis of these data has been optimized first.

The data has been preselected on the reaction $\mathrm{pd} \to {}^3\mathrm{He} + \mathrm{X}$ and at least one positive charged, one negative charged and two neutral particles detected in the central detector. Several hundreds of million events of possible background reactions have been simulated to describe the measured data in order to determine their contribution to the background. These simulations are not simple phase space but also include known physics models. For a correct description of the measured data contributions from random coincidences due to event overlap need to be considered as well. Fig. 2 shows a preliminary example fit of a data sample from the 2009 $\mathrm{pd} \to {}^3\mathrm{He}\eta$ beam time for the invariant mass distribution of two neutral particles. Additionally to the shown distribution further invariant mass spectra are fitted. The determined contributions of the different reactions will be used for cut optimization.

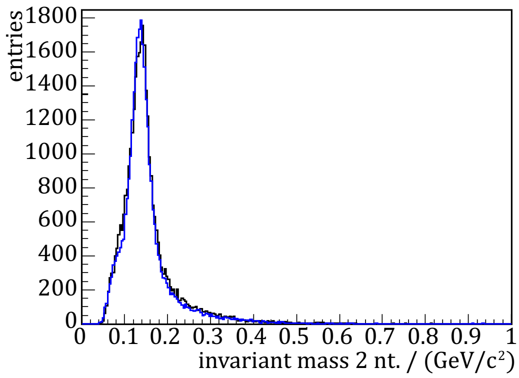

Figure 2: Invariant mass of two neutral particles detected in the central detector for the angular bin $0.8 < \cos\vartheta^{\mathrm{He}}_{\mathrm{cms}} \leq 1.0$. The data sample from the 2009 $\mathrm{pd} \to {}^3\mathrm{He}\eta$ beam time is shown in black. The fit using Monte Carlo simulations and events from random coincidences is shown in blue.

First test analyses of the proton proton data set give very promising results. Fig. 3 shows the missing mass of the two protons for a data sample which has been preselected on two charged and two neutral CD particles. Most remaining η-events origin from the decay $\eta \to \pi^0\pi^+\pi^-$ which will be rejected by further cuts. Currently the calibration of the various detectors is being checked and optimized further. Both the analysis of the ^{3}He and the proton data set are very sensitive to the decay channel of interest and capable to reach for lower relative branching ratios than the existing upper limit.

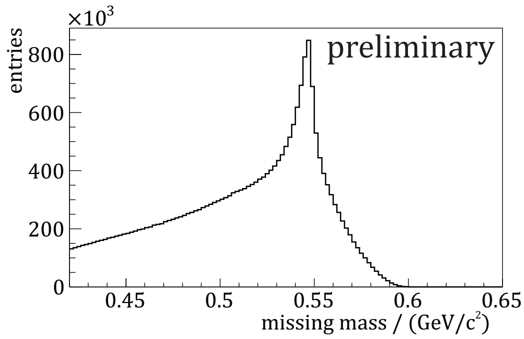

Figure 3: Missing mass of the two protons. The $\mathrm{pp} \to \mathrm{pp} + \mathrm{X}$ data sample has been preselected on two charged and two neutral CD particles.

References

[1] J. Smith, Phys. Rev. **166**, 1629 (1968).
[2] M.R. Jane *et al.*, Phys. Lett. B **59**, 99 (1975).

*Supported by COSY-FFE
†Institut für Kernphysik Westfälische Wilhelms-Universität, 48149 Münster, Germany

Studying the reaction pd → ^{3}Heπ^0 with WASA-at-COSY*

K. Sitterberg†, F. Bergmann†, K. Demmich†, N. Hüsken† and A. Khoukaz†

In 2014 a beam time using the WASA-at-COSY setup was performed to study total and differential cross sections of the pd → ^{3}Heη reaction at 15 different proton beam momenta ranging from $p_\mathrm{p} = 1600\,\mathrm{MeV/c}$ to $p_\mathrm{p} = 1740\,\mathrm{MeV/c}$. In order to determine the integrated luminosity for each energy the reaction pd → ^{3}Heπ^0 was chosen for normalization. This two-body reaction can be fully identified and reconstructed with measurement of the four momentum of the ^{3}He and the missing mass technique.

Since the normalization procedure relies on the differential cross sections in the very backward hemisphere of this reaction, a reasonable angular binning had to be determined. Based on both the detector resolution and the collected statistics 40 angular bins in $\cos\theta^{\pi^0}_{CMS}$ were chosen for first studies.

To account for the detector acceptance of the π^0 reaction, an acceptance correction was done by analyzing a sample of Monte Carlo generated events. The acceptance $A(\theta)$ was then calculated per beam momentum and angular bin as the ratio of the reconstructed and generated events, $A(\theta) = N^{\pi^0}_{rec}(\theta)/N^{\pi^0}_{gen}(\theta)$. An example is given in figure 1.

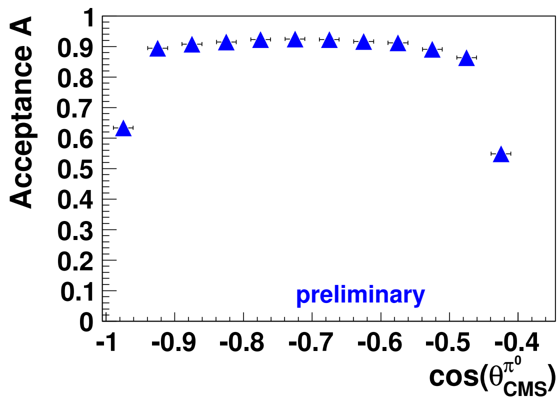

Figure 1: Detector acceptance for the normalization reaction $pd \to {}^3\mathrm{He}\pi^0$ for $p_\mathrm{p} = 1700\,\mathrm{MeV/c}$. The detector acceptance for this reaction vanishes for $\cos\theta^{\pi^0}_{CMS} > -0.4$.

The data normalization will be done in two steps. First, an absolute normalization and luminosity determination will be performed for the data with $p_\mathrm{p} = 1700\,\mathrm{MeV/c}$. In figure 2, differential cross sections for the pd → ^{3}Heπ^0 reaction at $\cos\theta^{\pi^0}_{CMS} = -1$ are shown for various beam energies T_p ranging from 500 MeV to 1400 MeV. Obviously, the differential cross section at a beam momentum of $p_\mathrm{p} = 1700\,\mathrm{MeV/c}$ (i.e. $T_\mathrm{p} \approx 1.0\,\mathrm{GeV}$) can be retrieved. Extrapolating the angular distribution of ^{3}Heπ^0 events (see figure 3) to $\cos\theta^{\pi^0}_{CMS} = -1$, in combination with the data shown in figure 2, allows the determination of the luminosity and thus for an absolute normalization. Currently, the presented analysis is performed with a much finer polar angle binning to improve the quality of the extrapolation shown in figure 3. After that, the second step is to perform a normalization relative to the $p_\mathrm{p} = 1700\,\mathrm{MeV/c}$ data for the remaining beam momenta.

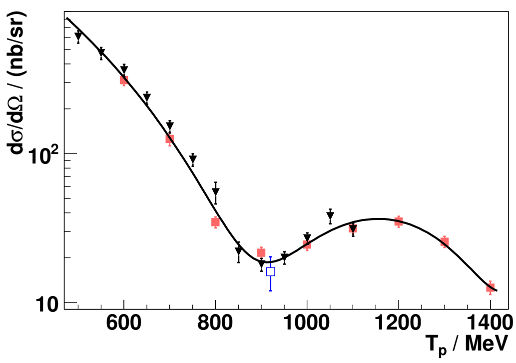

Figure 2: Differential cross sections at $cos\theta^{\pi}_{CMS} = -1$ for the reactions pd → ^{3}Heπ^0 (open square, [1]), pd → ^{3}Hπ^+ (filled squares, scaled by isospin factor 0.5, [1]), dp → ^{3}Heπ^0 (triangles, [2]) for different proton beam energies T_p. Data fitted by 5th order polynomial, error bars include statistical and systematic uncertainties. Taken from [3].

Applying this normalization to the data, it will be possible to extract both total and differential production cross sections for the reaction pd → ^{3}Heη.

In addition, the luminosity will be checked using different reactions, e.g. the quasi elastic pp-scattering.

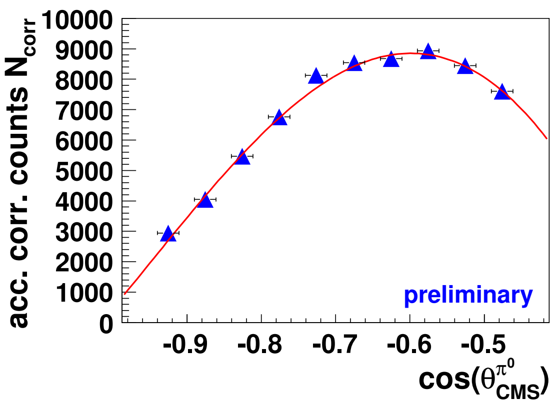

Figure 3: Acceptance corrected counts for $pd \to {}^3\mathrm{He}\pi^0$ at $p_p = 1700\,\mathrm{MeV/c}$. The red fit is a 4th order polynomial.

References

[1] P. Berthet *et al.*, Nucl. Phys. A **443**, 589 (1985).
[2] C. Kerboul *et al.*, Phys. Lett. B **181**, 28 (1986).
[3] P. Adlarson *et al.*, Eur. Phys. J. A **50**, 100 (2014).

*Supported by COSY-FFE and the European Union Seventh Framework Programme (FP7/2007-2013) under grant agreement n 283286

†Institut für Kernphysik, Westfälische Wilhelms-Universität, 48149 Münster, Germany

ToPix 4 Readout System and Test Beam Measurements

Simone Esch

The $\overline{\mathrm{P}}$ANDA experiment will deal with very high interaction rates up to 2 $\times 10^7$ interactions/s. Since the MVD is the innermost detector it has to handle a high flux of particles. In the "hottest" areas of the MVD a pixel front end module has to handle an average particle rate of up to 2.9 $\cdot 10^6$counts/s for a full size front end ASIC. The peak rate will be even more than 4 $\cdot 10^6$counts/s. Due to the trigger less readout concept of $\overline{\mathrm{P}}$ANDA the full data stream of the MVD has to be read out which is a novel and challenging feature for this kind of detector.

An ASIC is under development for the readout of the silicon-pixel part of the MVD detector. The recent version of this ASIC is the Torino Pixel 4 (ToPix 4). The ToPix 4 is a reduced size prototype with 640 pixels arranged in four double-columns, filling an area of 20 times 32 pixels. The final ASIC will have 12,760 pixels arranged in 55 double-columns with 116 pixels per column.

The ToPix 4 sends for every time interval passed a frame word. This leads to a continuous stream of data during operation. Hit words are send within these frames. Each frame is numbered which gives the possibility to define a global time stamp for every hit.

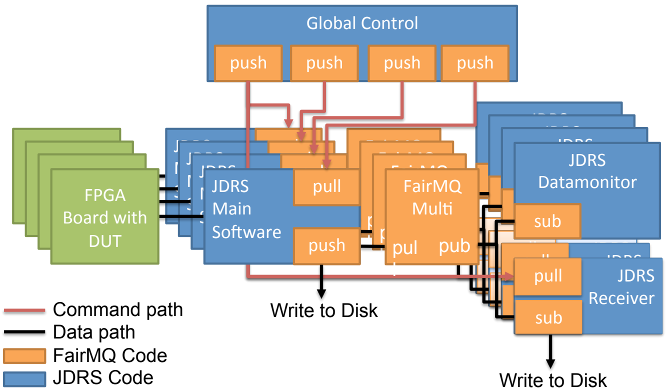

Fig. 1: Data and command paths in the JDRS software. Data from the FPGA readout board are written to disk and send to a FairMQ multiplier. From this multiplier different software has access to the data like a monitoring program or backup program for online backup of the data. A global control software sends start/stop commands to all devices.

To readout ToPix and other ASICs the Jülich Digital Readout System (JDRS) has been developed and was now adapted to work with ToPix 4. To deal with the continuous data stream of the ToPix 4 and parallel readout of four ToPix ASICs for test beam measurements the JDRS has been enhanced with the FairMQ transport layer. FairMQ is a development for the FairRoot analysis framework and is a message queue based transport layer using ZeroMQ or nanomsg. Using FairMQ and message queues has various benefits. FairMQ gives the possibility to analyze the received data directly in the FairRoot or PandaRoot analysis framework. Message queues give the possibility to decouple tasks in the software e.g. recording to disk and monitoring the data stream. At the same time workload like analyzing the data can be spread over different threads or hosts.

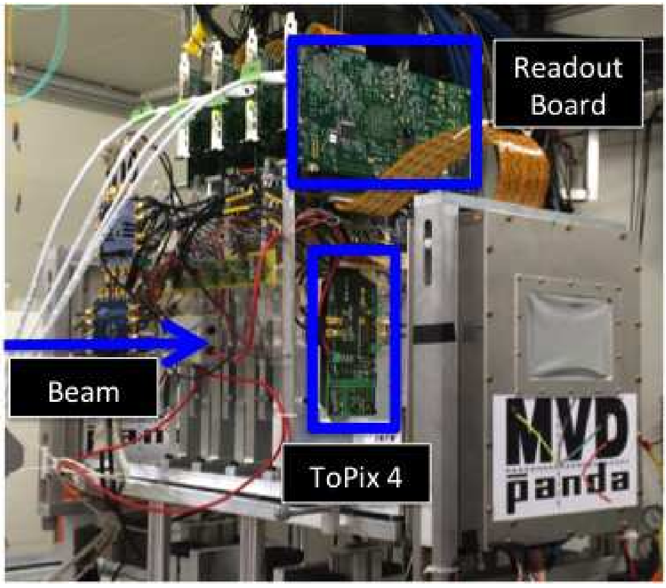

Fig. 2: Photograph of the test beam setup of four ToPix 4 prototypes (center PCB) and the JDRS readout boards (upper PCB). The ToPix 4 are arranged as a beam telescope. The proton beam is coming from the left side.

Figure 1 shows the structure of the JDRS software used for ToPix 4 measurements. The JDRS main software runs a FairMQ socket which collects the data from the FPGA board, saves it to disk and wraps it in a FairMQ message. The message is send to a FairMQ multiplier. The multiplier has several FairMQ output sockets where other FairMQ based programs can connect and receive the FairMQ messages and the hit data. For the test beam measurement a monitoring program (JDRS Datamonitor) and an online backup program (JDRS Receiver) have been created and used. The recording to disk of the main program and the receiver are synchronized via the global control software, which sends commands to the different program parts.

The upgraded software has been successfully used in the test beam for the readout of four ToPix ASICs in a beam telescope setup. Figure 2 shows a picture of the test beam setup. The test beam should confirm generel aspects of the ToPix 4 and show the high rate capabilities of the ASIC. Due to the global time stamp and the beam telescope setup tracking of particle tracks is possible. The test beam was done with a proton beam with p_{Beam}=2.95 GeV/c at the Jessica area at COSY.

Various measurements have been done during this test beam and the analysis of this data is ongoing.

Figure 3 shows the hit data displayed as a function of the global time stamp for a single ToPix 4. The picture shows the time structure of the particle beam consisting of time with and without hits on the sensor. The structure is created by the extraction of the beam from COSY to the test beam site and a pause after that (a spill). The measurement was done for ca. 13 minutes, covering 9 spills of the proton beam.

Figure 4 shows the hitmap of a single ToPix 4. The beam spot is visible in the upper part of the hitmap. due to the

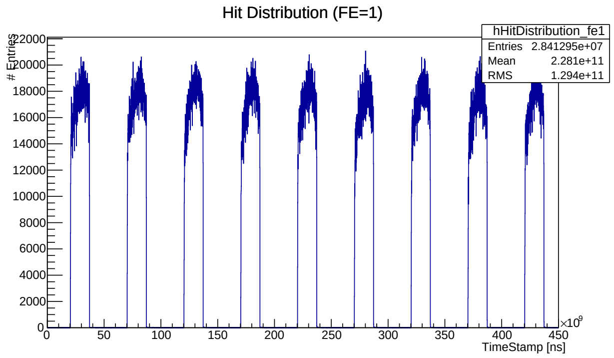

Fig. 3: Histogram of hit data measured by ToPix 4 as a function of the global time stamp. In the historgram the ten individual spills are clearly visible.

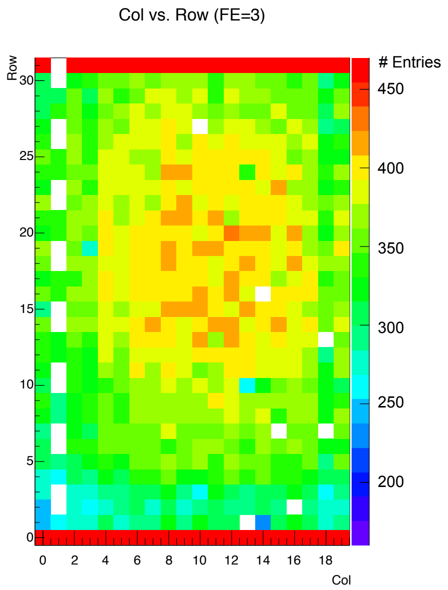

Fig. 4: Hitmap of a ToPix 4 during the test beam. In the center part the beam spot is visible. The pixels in the first and the last row are connected to a sensor area which is twice as large as for other pixels, due to this they see a higher amount of hits.

higher amount of entries. Nearly all pixels are working as expected. The pixels of the first and the last row are connected to a sensor area which is twice as large as for the other pixels. Thus these pixels see the double amount of hits compared to the other pixels.

The data of the test beam is still under investigation, but the first results show that the prototype with the JDRS setup is properly working at 50 MHz clock frequency. The next test beam in 2015 will focus on the performance of ToPix 4 with the JDRS at the aim frequency of 160 MHz.

Systematic studies of spin dynamics at COSY in preparation for the EDM searches*

A. Saleev[a] for the JEDI collaboration

Searches of the electric dipole moment (EDM) at storage rings encounter strong background coming from magnetic dipole moment (MDM). Both in pure electric and pure magnetic, and also combined E/B rings, one of the complexity is MDM spin precession in radial and longitudinal imperfection magnetic fields, which contribute to systematic effects that mimic EDM signal.

The goal of current systematic studies is to find a way for disentangling the EDM signal and MDM-induced imperfection spin rotation. In a pure magnetic ring, like COSY, the generic signal of the EDM is spin rotation in the radial motional electric field. This electric field can be considered as an imperfection field as well. To study the systematic effects of the imperfection fields we proposed an original method which makes use of the two static solenoids acting as artificial imperfections. At COSY, there are two e-coolers, located opposite to each other at straight sections. A set of compensation solenoids from new (2 MeV) e-cooler can produce total field in the range $\int B_1 dl = [-28\ldots 28]\,Tmm$, and solenoids in old e-cooler $\int B_2 dl = [-154\ldots 14]\,Tmm$. When the solenoids in one of the coolers are set up on a specific current, they produce a spin kick $\chi_i = \frac{1+G}{B\rho}\int B_i dl$ around longitudinal axis. During the beam cycle, the solenoids in both e-coolers have been switched on simultaneously at 20 seconds after the spin-flip of vertical polarization into horizontal plane, and then swtiched off at 45 seconds. Perturbation of the spin tune $\Delta\nu_S$ relative to the spin tune when solenoids are switched off, $\nu_S = Q_S$, is given by:

$$
\begin{aligned}
&-\sin(\pi Q_S)\Delta\nu_S \cong \qquad (1)\\
&\quad(1+\cos(\pi Q_S))\sin^2\left(\tfrac{y_+}{2}\right) - \tfrac{1}{2}(c_3+c_3^*)\sin(\pi Q_S)\sin y_+\\
&\quad-(1-\cos(\pi Q_S))\sin^2\left(\tfrac{y_-}{2}\right) + \tfrac{1}{2}(c_3-c_3^*)\sin(\pi Q_S)\sin y_-
\end{aligned}
$$

where the solenoid's spin kicks are defined as

$$
y_\pm = \frac{\chi_1 \pm \chi_2}{2}. \qquad (2)
$$

c_3 is longitudinal projection of spin closed orbit at location of solenoid 1 (2 MeV e-cooler), c_3^* is corresponding value for the solenoid 2 (old e-cooler):

$$
\vec{n}_{co} = c_1\vec{e}_x + c_2\vec{e}_y + c_3\vec{e}_z
$$
$$
\vec{n}^*_{co} = c_1^*\vec{e}_x + c_2^*\vec{e}_y + c_3^*\vec{e}_z
$$

Spin closed orbit is a unit vector of spin precession axis, given at some point of the ring, for the particle on closed orbit. The values of spin closed orbit in eq. (1) define the systematic effect of all imperfections present in the ring, except for the spin kicks from the e-cooler's solenoids itself. $c_3 \neq c_3^*$ because of non-commuting property of spin rotations. In case of no imperfections present in the ring, $c_3 = c_3^* = 0$ and spin tune $\nu_S = G\gamma$ (G is the anomalous magnetic moment, and γ the relativistic Lorentz factor). Multiple measurements of spin tune shift $\Delta\nu_S$ with respect to the spin kicks by the solenoids, y_+, y_-, produce spin tune map (see Fig. 1). Fitting the data points in Fig. 1 to function (1) gives the values $c_3 = -0.00299124 \pm 1.8 * 10^{-7}$, $c_3^* = -0.00163653 \pm 7.1 * 10^{-8}$ and locates a saddle point in two-dimensional map $\Delta\nu_S(y_+, y_-)$ (see Fig. 2).

Analysis of possible systematic effects coming from the changes of closed orbit when the solenoids are switched on is ongoing. During JEDI beamtime at September 2014, two spin tune maps have been measured, with time span 24 hours. The values obtained for c_3 and c_3^* are consistent for both maps. Assuming no other significant systematic effects, the expirement regards as first direct measurement of spin closed orbit at COSY with unprecedented precision of 10^{-7}.

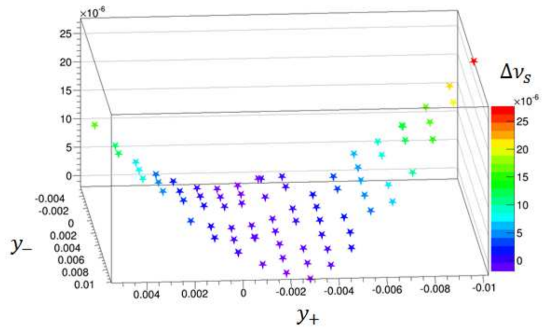

Fig. 1: Spin tune map. Each data point represent single measurement of $\Delta\nu_s(y_+, y_-)$ for deuterons at $T = 270$ MeV, and an unperturbed spin tune $Q_S = -0.160971917$. Error bars are smaller then size of symbols.

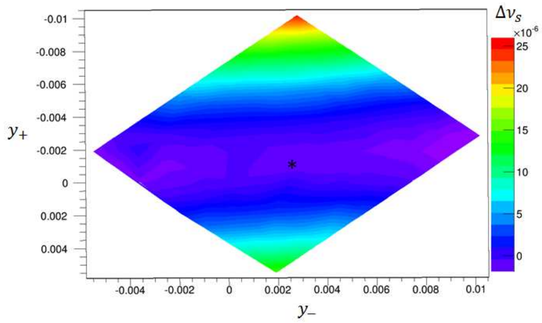

Fig. 2: View from the top on the spin tune map. The data points are connected with color levels representing $\Delta\nu_s$. Location of the saddle point has been determined from fit, $a_+ = -0.00111077 \pm 6.1 * 10^{-8}$ *rad* and $a_- = 0.00244326 \pm 2.05 * 10^{-7}$ *rad*, marked by star.

[a] Institut für Kernphysik, Forschungszentrum Jülich, Germany, and Landau Institute, Chernogolovka, Russia.

* supported by the COSY–FFE program under contract number COSY-125.

Systematic Error Investigation of the Spin Tune Analysis for an EDM Measurement at COSY

F. Trinkel[a,b] for the JEDI collaboration

This report describes the method how data are simulated for a systematic error investigation for the spine tune determination ν_s and discusses possible systematic errors due to acceptance and polarization variations.

The goal of the JEDI collaboration is to measure an EDM (Electric Dipole Moment) of charged particles (p,d and ^3He). A first step on the way for an EDM measurement is the investigation of systematic errors at the storage ring COSY. One part for these studies examines the spin tune ν_s of an horizontally polarized deuteron beam. The spin tune is defined as the number of spin rotations in the horizontal plane relative to the particle turn. To a first approximation the spin tune is given by $|\nu_s| \approx \gamma G$, where γ is the Lorentz factor and G is the anomalous magnetic moment of the particle.

For the spin tune measurement the bunched beam is slowly extracted on a solid carbon target and the time of every event of an elastic scattered deuteron is recorded with EDDA detector. A sketch of the EDDA detector is shown in figure 1, where the four coloured detector-areas illustrate the different counting areas for scattered particles.

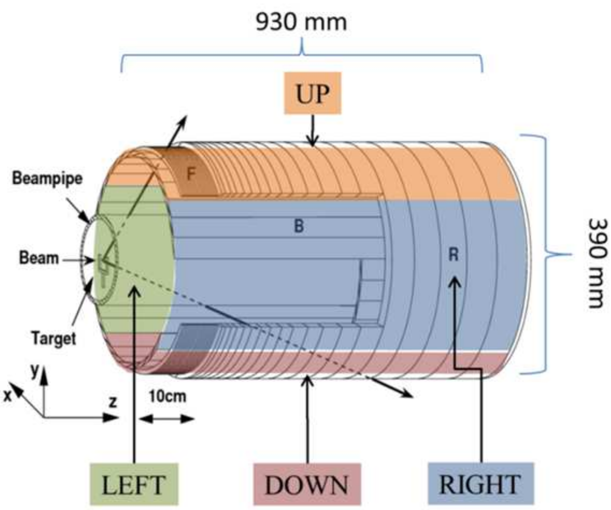

Fig. 1: Sketch of the EDDA dector. The four coloured detector-areas define the different counting areas for scattered particles.

To calculate an asymmetry related to the polarization of the beam, the rates in opposite detector areas (e.g. up and down) are counted. For a deuteron beam with a momentum of $p_d = 0.97\,\text{GeV/c}$ the revolution frequency is approximately $frev \approx 750\,\text{kHz}$, which leads to an horizontal spin precession frequency of

$$f_s = |\nu_s \cdot| f_{rev} \approx |\gamma G_d| f_{rev} \approx 120\,\text{kHz}, \tag{1}$$

with $\gamma = 1.125$ and $G_d = -0.143$. The detection rate is of the order of 5 kHz for a beam with 10^9 particles per fill. The counting rates for the scattered particles in the up- and down-detector are shown in equations 2 and 3,

$$N_{up}(t) = a_{up} \cdot N(t) \cdot n\sigma \left[1 + P(t) A_{up} \cdot \sin(2\pi f_s t + \phi_{up})\right] \tag{2}$$

$$N_{dn}(t) = a_{dn} \cdot N(t) \cdot n\sigma \left[1 - P(t) A_{dn} \cdot \sin(2\pi f_s t + \phi_{dn})\right] \tag{3}$$

where the acceptance $a_{up,dn}$, number of target particles n and the analysing power $A_{up,dn}$ are detector parameters. The number of beam particles $N(t)$, the unpolarized cross section σ and the polarization $P(t)$ are beam parameters. Around $5 \cdot 10^5$ particles are detected in a cycle of 100 s.

The simulation program calculates time values t in a range of 0 to 100 s in dependency of a cross-section $\sigma_{up,dn}$. The mathematical context is shown in equation 4. The value $a_{up,dn}(1-\varepsilon_2 t)$ respects a linear decrease of the acceptance for a given decreasing-factor ε_2 . The constant $C_{up,dn}$ is the product of polarization $P_{up,dn}$ and analysing power $A_{up,dn}$ and decreases with the time by a given decreasing-factor ε_1.

$$\sigma_{up,dn}(t) = \begin{cases} a_{up}(1-\varepsilon_2 t)\left[1 + C_{up}(1-\varepsilon_1 t)\sin(2\pi f t + \phi)\right] \\ a_{dn}(1-\varepsilon_2 t)\left[1 - C_{dn}(1-\varepsilon_1 t)\sin(2\pi f t + \phi)\right] \end{cases} \tag{4}$$

To create simulated data three random number generators are used. The first one is an uniform number generator, which generates values t in an interval from 0 to 100 s. The second and third random number generator generate uniform numbers x_1 and x_2 in an interval from 0 to 1. The generated time value t is used to calculate the up- and -cross-section. With this cross-section a probability P_{up} is calculated (equation 5) to find an event for the upper detector.

$$P_{up} = \frac{\sigma_{up}}{\sigma_{up} + \sigma_{dn}} \tag{5}$$

The generated time value t belongs to an event in the upper detector, if $P_{up} \leq x_1$ and $x_2 > a_{up} \cdot (1-\varepsilon_2 t)$. If $P_{up} > x_1$ and $x_2 > a_{dn}(1-\varepsilon_2 t)$, than the generated time value belongs to an event in the down detector. The dependency $x_2 > a_{up,dn}(1-\varepsilon_2 t)$ respects influence of the linear changes in the detector acceptance. This algorithm is for one data setup repeated as long as $5 \cdot 10^5$ time values are generated. The input parameters for the simulations are given in table 1. These parameters have the same property than a polarized deuteron beam at COSY.

Table 1: Input parameters for the values of equation 2 and 3. The parameter values are in the same region as measured values for a deuteron beam at COSY.

Input parameter	up	dn
a [%]	100	100
C [%]	25	25
f [kHz]	120	120
ϕ [rad]	0	0
$\varepsilon_1 [s^{-1}]$	0.01	0.01
$\varepsilon_2 [s^{-1}]$	0.01	0.01

The values of the parameters in table 1 are used to simulate three different data sets to investigate possible systematic effects of acceptance and polarization changes. An illustration of the three simulated scenarios is shown in figure 2. The first case shows a linear decrease in polarization C over time and the acceptance a stays constant. In the second case the polarization C and acceptance a decrease linear over time. The last case reflects a linear decrease in polarization C and a linear increasing acceptance for the up-detector a_{up} and a linear decreasing for the down-detector a_{dn}.

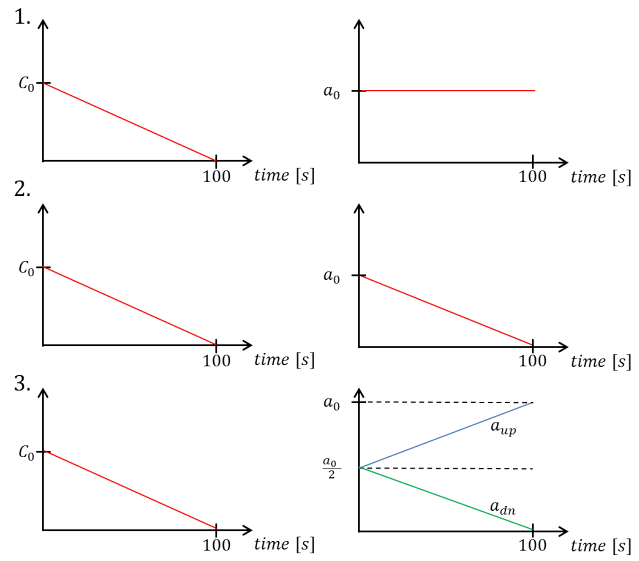

Fig. 2: Illustration of the three possible simulated scenarios. The first case shows a linear decrease in polarization C over time and the acceptance a stays constant. In the second case the polarization C and acceptance a decreases linear over time. The last case reflects a linear decrease in polarization C and a linear increasing acceptance for the up-detector a_{up} and a linear decreasing for the down-detector a_{dn}.

A detailed description of the spin tune analysis can be found in [1, **?**]. The figures 3 to 6 show the interpolated spin tune of the applied spin tune analysis for the up- and down detectors together. To compare the results of the interpolated spin tune for the different cases, one data set was simulated with constant polarization C and acceptance a over the whole time. This result is shown in figure 3. It can be seen, that the smallest error for $\Delta\nu$ lays in the order of 10^{-10}. The interpolated spin tune for the data sets, which are presented in figure 2, show, that a linear decreasing polarization C or acceptance a do not influence the spin tune analysis. The smallest error for the interpolated spin tune $\Delta\nu$ for each simulated case is in the order of 10^{-10}. This gives the conclusion, that systematic effects of changes in polarization and acceptance do not influence the method, how the spin tune is calculated.

[a] IKP FZJ, Germany
[b] RWTH Aachen University, Germany

References:

[1] D. Eversmann, Annual Report 'Spin Tune Determination of Deuteron Beam at COSY' (2013)

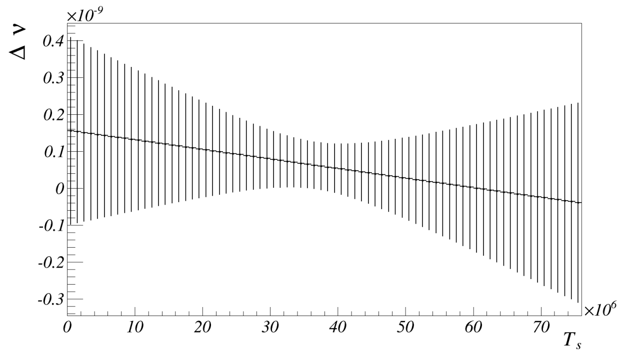

Fig. 3: Interpolated spin tune analysis of data with constant acceptance a and polarization C.

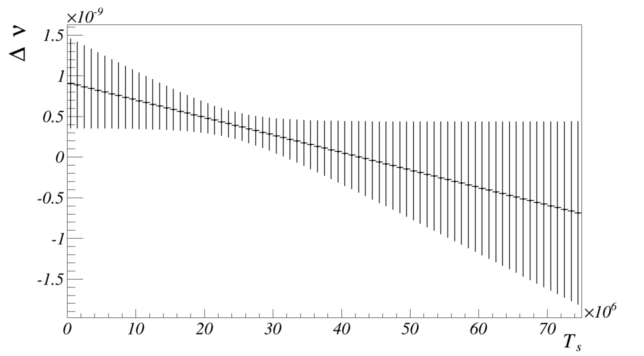

Fig. 4: Interpolated spin tune analysis of data with constant acceptance a and decreasing polarization C.

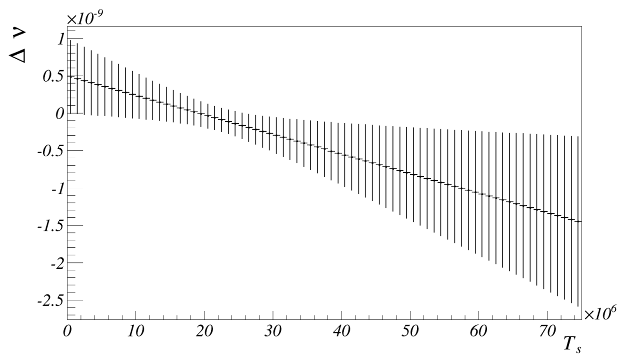

Fig. 5: Interpolated spin tune analysis of data with decreasing acceptance a and polarization C.

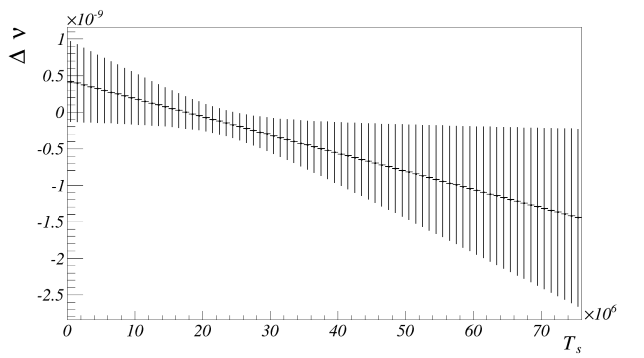

Fig. 6: Interpolated spin tune analysis of data with increasing acceptance a_{up}, decreasing acceptance a_{dn} and polarization C.

Development of a new control framework for lattice parameter calculations and particle tracking

M. Rosenthal[a,b] for the JEDI-Collaboration

Spin motion of relativistic particles in electromagnetic fields is described by the Thomas-BMT equation [1, 2]. In presence of an magnetic and electric dipole moment, this equation can be expressed in the following form [3]:

$$\frac{\mathrm{d}\vec{s}}{\mathrm{d}t} = \vec{s}\times\vec{\Omega}_{MDM} + \vec{s}\times\vec{\Omega}_{EDM}, \tag{1}$$

$$\vec{\Omega}_{MDM} = \frac{q}{\gamma m}\left[(1+G\gamma)\vec{B} - \frac{G\gamma^2}{\gamma+1}\vec{\beta}(\vec{\beta}\cdot\vec{B}) - \left(G\gamma+\frac{\gamma}{\gamma+1}\right)\frac{\vec{\beta}\times\vec{E}}{c}\right],$$

$$\vec{\Omega}_{EDM} = \frac{\eta}{2}\frac{q}{mc}\left[\vec{E} - \frac{\gamma}{\gamma+1}\vec{\beta}\left(\vec{\beta}\cdot\vec{E}\right) + c\vec{\beta}\times\vec{B}\right].$$

The study of the feasibility of concepts for storage ring based EDM measurements powerful simulation codes for lattice calculations and tracking of spin motion through the electromagnetic field configurations are necessary. These codes often needs to be extended to the specific requirements. One of the used codes is COSY Infinity [6], which is based on a differential algebraic approach. Given the analytic electromagnetic field distribution of an element, it calculates the corresponding transfer map for phase space and spin motion and allows for fast repetitive tracking of particle coordinates through these maps. For the systematic investigation of the proposed EDM measurement method at COSY, this code was extended by the EDM contribution to spin motion according to equation 1. Furthermore the calculation of time-dependent fields was introduced.

An efficient production and analysis for different simulation tasks require a powerful handling of the input and output data of these codes. On the input side, several simulation tasks often require identical code segments. Variation of parameters based on preceding results must be possible. On the output side, tracking results must be stored efficiently and easily accessible for following analysis routines. A new C++ based framework was developed to take care of these requirements. Each accelerator element is described in a corresponding class and inherits the required parameter, i.e. length

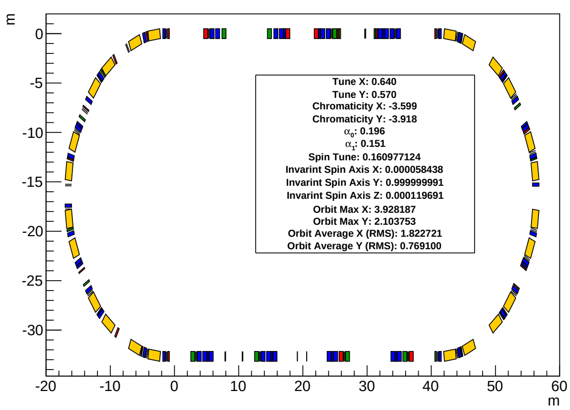

Fig. 1: Schematic view of the COSY accelerator with lattice parameters, i.e. fractional tune, chromaticity, momentum compaction factor and spin tune. The guiding dipole magnets are shown in yellow, multipole in blue, correctors and beam position monitors in red and green.

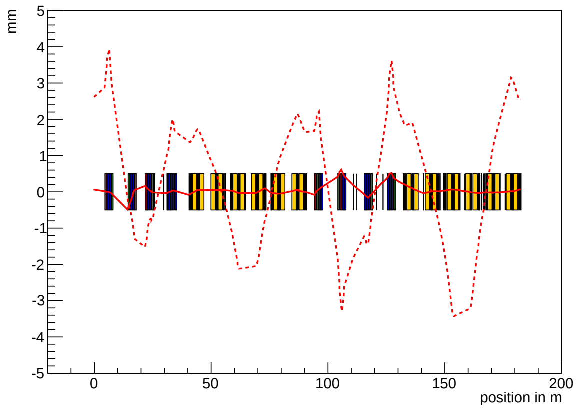

Fig. 2: Horizontal Orbit for randomly Gaussian distributed radial and vertical shifts of the quadrupole magnets ($\sigma = 0.1$ mm) before (dashed) and after (solid) orbit correction.

and field strength. Several elements of the same type can be assigned to families to allow for the modification of parameters on family basis. Furthermore misalignment parameters for shifts and rotations are introduced. All elements can be combined to a full beam line.

A beam line is mandatory for the so called task classes. One of these task classes is the "Calculator". It accesses the defined beam line and can be used to calculate the transfer maps of all elements parallelized. For this purpose the definitions of the C++ classes are automatically converted into COSY Infinity source code and executed. The maps are stored on disk and are loaded to calculate ring parameters like betatron tunes, chromaticities, momentum compaction factors, the spin tune, as well as the closed orbit assuming an repetitive beam line. Several classes of the ROOT framework [7] are used to store and to illustrate the results. An example for the COSY accelerator is shown in Fig. 1. Here a deuteron beam with $p = 970$ MeV/c and randomly Gaussian distributed radial and vertical shifts of the quadrupole magnets ($\sigma = 0.1$ mm) were used. The corresponding closed orbit for the horizontal direction in this particular example is illustrated using a dashed line in Fig. 2 . The orbit diagnosis and correction system of roughly 60 beam position monitors (BPMs) and 40 steering correctors can then be used to minimize the closed orbit. For that purpose the orbit response matrix, which expresses the resulting orbit changes at the BPMs for a given corrector kick in linear order, is calculated. The C++ library Armadillo [8] for linear algebra operations is utilized for calculation of the pseudo-inverse of this matrix. Given the orbit offsets at the BPM locations, the pseudo-inverse can be used to retrieve the required corrector strengths to correct the orbit. For the given example the resulting orbit is shown in Fig. 2 by the solid line. Assuming the orbit offset with respect to the quadrupole centers is known, the corrector magnets can be used to correct these offsets. An interesting aspect is the RMS value of the orbit offset in all quadrupoles for different sizes of σ. The correlation of these two parameters is shown in Fig. 3 for 200 differ-

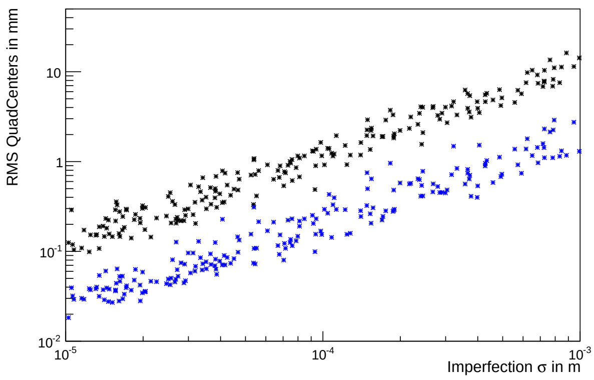

Fig. 3: RMS value of the orbit offset at quadrupole locations with respect to their magnetic center. Each point corresponds to a different set of randomly Gaussian distributed shifts of the quadrupoles with varying standard deviation. The black points are before orbit correction, the blue points after minimizing the RMS value using the existing correctors in the ring.

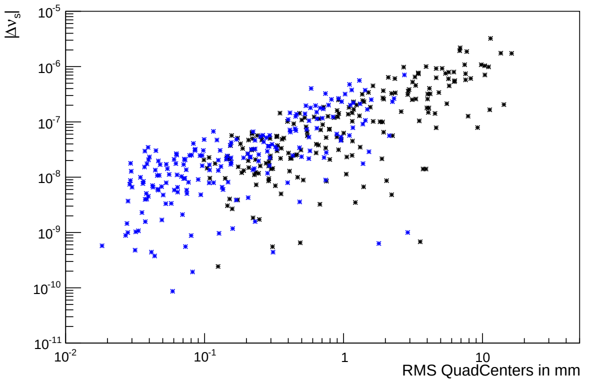

Fig. 4: Absolute value of the spin tune change for different sets of randomly Gaussian distributed shifts of the quadrupoles with varying standard deviation (see also Fig. 3). Black points are before and blue points after applied orbit correction.

ent σ-values The RMS value can be reduced by one order of magnitude using the correctors and the described algorithm in simulations.

In addition to the influence of beam motion, the impact of these misalignments on spin motion is of particular interest for EDM searches at COSY. An important parameter is the spin tune. It describes the number of spin revolutions with respect to the momentum vector. During the last year the spin tune could be measured to very high precision. Following the Thomas-BMT-equation the spin tune in an ideal magnetic ring is given by $\nu_s = G\gamma$. Imperfection fields introduce non commuting spin rotations and might change the spin tune. Fig. 4 shows the spin tune change in connection to the RMS value of the orbit offset in the quadrupole centers. The previously defined random misalignments were used. To allow for a logarithmic scale the absolute value of the spin tune change is presented. For an RMS value of 1 mm the spin tune change is in the order of 10^{-7}.

A second important task class is the "Tracker". It allows for setting up a particle tracking job processed by COSY Infinity. In the following example the EDM related buildup in presence of an RF-E×B-dipole is presented. The method is described in [4, 5]. Deuterons with $p = 970\,\mathrm{MeV/c}$ on the closed orbit were examined. Their spin vector was initially aligned to the invariant spin vector of the ring in presence of no radiofrequency field. The RF-E×B-dipole with a length of 0.6 m was then turned on with a magnetic field of $B = 0.1\,\mathrm{mT}$ and a corresponding electric field to cancel the Lorentz force within this device. Its frequency was adjusted to the spin precession frequency in the rest of the ring to create an intrinsic spin resonance. The resulting buildup in presence of an EDM with $\eta = 10^{-4}$ is shown in Fig. 5. Only every 1000th turn is displayed. This study reveals the slow buildup of an polarization as soon as the RF-device is running on spin resonance. The buildup rate scales linearly with the field strengths and the magnitude of the EDM as shown in Fig. 6. In an ideal ring and an ideal RF-device this would allow to extract the

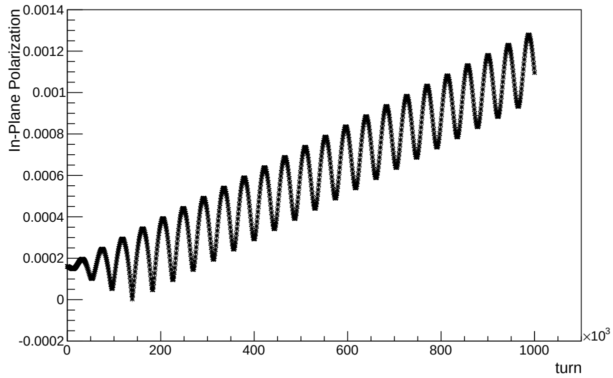

Fig. 5: Buildup of In-Plane-Polarization for deuterons on the closed orbit with momentum of $p = 970\,\mathrm{MeV/c}$ and an EDM corresponding to $\eta = 10^{-4}$. The buildup was created in presence of an RF-E×B-dipole with $B = 0.1\,\mathrm{mT}$ and $l = 0.6\,\mathrm{m}$. The spin of the particle was aligned to the invariant spin axis at turn zero. Every 1000th turn is shown.

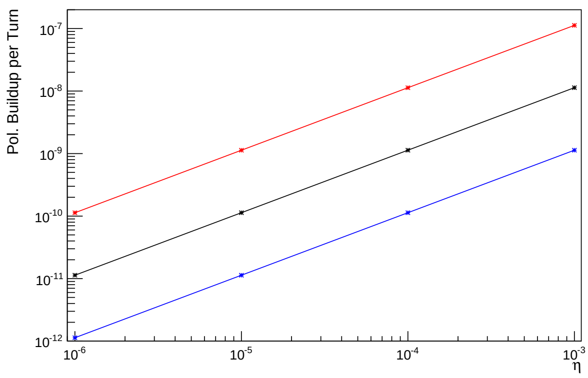

Fig. 6: Polarization buildup for different EDM sizes and RF-E×B-dipole stengths assuming deuterons on the closed orbit with momentum of $p = 970\,\mathrm{MeV/c}$. The length of the RF-E×B-dipole was $l = 0.6\,\mathrm{m}$ and the magnetic field $B = 0.01\,\mathrm{mT}$ (blue), $B = 0.1\,\mathrm{mT}$ (black) and $B = 1\,\mathrm{mT}$ (red). The electric field was adjusted accordingly to cancel the Lorentz force within this device.

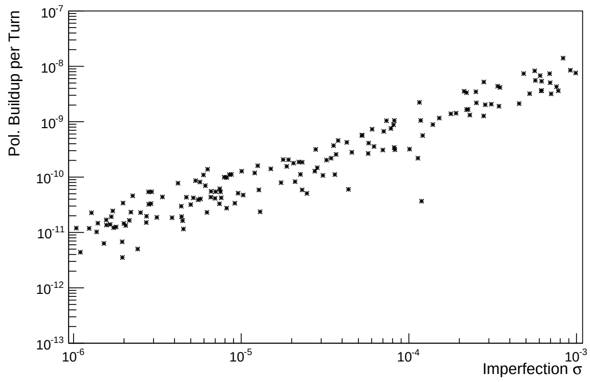

Fig. 7: Buildup of In-Plane-Polarization for deuterons on the closed orbit with momentum of $p = 970\,\mathrm{MeV/c}$ and no EDM, but randomly Gaussian distributed vertical shifts of the quadrupole magnets using different standard deviations. The buildup was created in presence of an RF-E×B-dipole with $B = 0.1\,\mathrm{mT}$ and $l = 0.6\,\mathrm{m}$ and correspondigly chosen electric field to cancel the Lorentz force.

EDM by measuring the polarization buildup. Imperfections in a non ideal ring can mimic an EDM and also lead to a polarization buildup. To illustrate the magnitude of these buildup vertical shifts of the quadrupoles were introduced. Random Gaussian distribution of these errors with varying standard deviation were examined. According to equation 1 these radial Imperfection fields lead to spin rotations around radial axis similar to the EDM contribution in the motional electric field $\vec{\beta} \times \vec{B}_y$. Fig. 7 illustrates the buildup for different amounts of misalignments. Without correction vertical quadrupole shifts distributed with $\sigma = 0.1\,\mathrm{mm}$ mimic an EDM buildup corresponding to $\eta = 10^{-4}$. In further studies orbit correction schemes and algorithms will be tested to surpress the systematic limitation arising from misalignments in the ring. The developed framework is an excellent basis for the investigation of these studies.

References:

[1] L. H. Thomas, Phil. Mag. 3, 1 (1927)

[2] V. Bargmann, L.Michel, V. L. Telegdi, Phys. Rev. Lett. 2 (1959), p. 435-436

[3] T. Fukuyama and A. J. Silenko, Int. Journal of Modern Physics A 28 (2013), 1350147

[4] F. Rathmann, A. Saleev and N. N. Nikolaev, Journal of Physics: Conference Series 447 (2013), p. 012011

[5] W. Morse, Y. Orlov, Y Semertzidis, Phys. Rev. ST Accel. Beams 16 (2013), p. 114001

[6] K. Makino and M. Berz, Nucl. Inst. & Meth. in Phys. Res. A 558 (2006), p. 346-350

[7] R. Brun and F. Rademakers, Nucl. Inst. & Meth. in Phys. Res. A 389 (1997), p. 81-86

[8] C. Sanderson, Armadillo: An Open Source C++ Linear Algebra Library for Fast Prototyping and Computationally Intensive Experiments. Technical Report, NICTA (2010)

[a] IKP FZJ, Germany
[b] RWTH Aachen University, Germany

Wien Filter studies in MODE

S. Chekmenev[a] for the JEDI collaboration

Number of simulations were performed with newly developed code MODE [1] in order to investgate the impact of different systematic errors for the precursor EDM experiment [2]. The RF Wien filter method was taken as a basis for the simulations. The main principle says that the RF Wien filter should have a radial electric E_x and a vertical magnetic B_y field, and it must be operated on a harmonic K of the spin motion,

$$f_{WF} = |K + G\gamma| f_{rev}, \tag{1}$$

where f_{WF} is the frequency of the harmonically excited RF Wien filter and f_{rev} is the beam revolution frequency.

The impact of the rotations of the Wien filter was investigated. Firstly, the EDM-like signal was generated by the MDM interaction with the rotated vertical magnetic field of the Wien filter. Secondly, the situation with the pure EDM build-up for the untilted device was considered. It was shown that the rotations of the RF Wien filter around the longitudinal axis yields the same build-up of the vertical polarization as caused by the EDM interaction with the motional electric field in COSY ring. See figure 1.

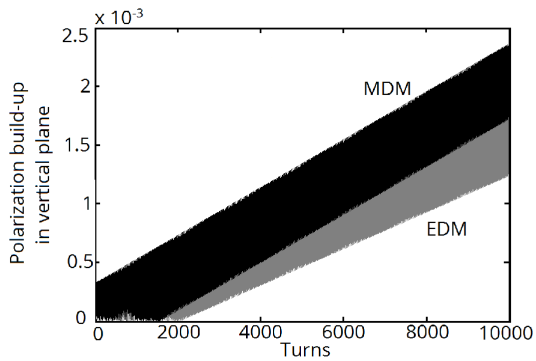

Fig. 1: The polarization build-up in vertical plane. The initial spin direction of the deuteron is longitudinal. In black: the MDM interaction with the field of the longitudinally rotated Wien filter in the absence of the EDM. The rotation angle is 10^{-4}rad. In grey: the EDM interaction with the motional electric field, when the Wien filter is perfectly aligned. An EDM of $2.6 \cdot 10^{-19} e \cdot$cm was assumed.

The spin motion was examined when the misalignments and rotations of the magnets of COSY took place. Two types of tracking were performed for that reason, one with the EDM and a perfect orbit and another without one for the distorted case. Two polarization build-up's were plotted against the turn number for both situations. The one with misalignments was compared to another one with the presence of the EDM in order to get the systematic limit on the current COSY configuration.

The mismatch between the operating frequency of the RF Wien filter and the spin resonance frequency was considered. Four particular situations with different relative frequency mismatches were tested in the simulation. The resulting polarization build-up's were compared. The deviation from linear behaviour, which prevents the possibility of polarization

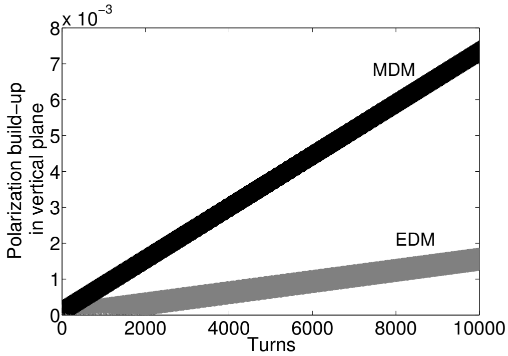

Fig. 2: The polarization build-up in vertical plane. The initial spin direction of the deuteron is longitudinal. In black: The polarization build-up due to the MDM interaction with imperfection fields of the misaligned magnets with RF Wien filter on. In grey: the EDM interaction with the motional electric field in the absence of imperfections. The EDM was $2.6 \cdot 10^{-19} e \cdot$ cm.

measurements, was demonstrated. It was presented that one must pay significant attention to the fullfilment of the resonance condition.

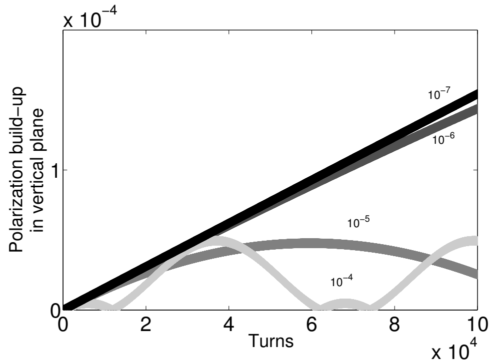

Fig. 3: The polarization build-ups due to the EDM interaction with the motional electric field for different values of the mismatch between the spin resonance and the operating Wien filter frequencies. a) $\Delta = 10^{-7}$ b) $\Delta = 10^{-6}$, c) $\Delta = 10^{-5}$, d) $\Delta = 10^{-4}$. An EDM was equal to $2.6 \cdot 10^{-21} e \cdot$cm.

In summary, all three simulation results indicate the same systematic limit, for the present situation at COSY, of the order of $10^{-19} e \cdot$cm. This is a starting point for the precursor experiment that is planned to be cunducted in the next 2 years. Based on this, one should think of an installation of a modern orbit correction system and on a way to control and keep the frequency of the RF Wien filter with the maximum achievable precision. Further simulation work will be done towards the implementation of an orbit correction algorithm in MODE program. Field errors of the Wien filter must be considered and the effect caused by them should be calculated.

[a] III. Physikalisches Institut, RWTH Aachen

References:

[1] A. Ivanov, Matrix Integration of ODEs for Spin-orbit Dynamics Simulation, in *Proc. 5th Int. Particle Accelerator Conf. IPAC2014*, eds. C. Petit-Jean-Genaz, G. Arduini, P. Michel, V. RW Schaa, Dresden, Germany(2014), p. 400

[2] A. Lehrach, J. Pretz, F. Rathmann *et al*, Search for Permanent Electric Dipole Moments at COSY. Step 1: Spin coherence and systematic error studies, 2014

Upgrade of the Low Energy Polarimeter Read-Out

Nils Hempelmann for the JEDI Collaboration*

1 Low Energy Polarimeter

The low energy polarimeter [1] measures the polarization of proton and deuteron beams prior to the injection into the COSY ring at kinetic energies up to 45 MeV for protons and 75 MeV for deuterons. The measurements can be used to optimize the settings of the polarized particle source independently from the ring. The particles are scattered off a fixed target made of carbon (C) or polyethylene CH_2. They are detected using twelve plastic scintillators. The scintillators are installed in groups of three at azimuth angles of 0°, 90°, 180° and 270°. Within each group the scintillators are spaced 10° of polar angle apart. The polar angle can be varied between 25° and 70° in the forward region and between 110° and 155° in the backward region.

Elastic and inelastic channels can be distinguished using the pulse height of the scintillator signals. For reactions for which the recoil particle can be detected, the time between the arrivals of the two outgoing particles is measured. This provides additional information about the particles' time of flight.

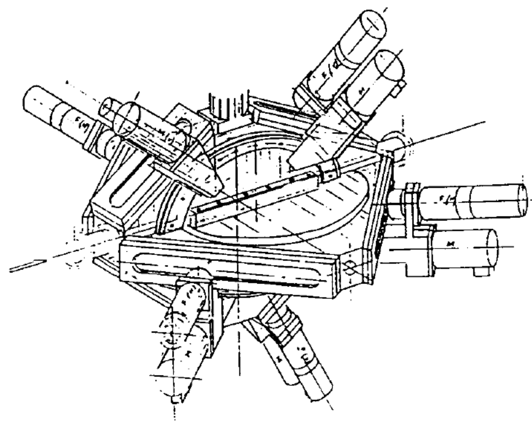

Figure 1: Schematic view of the low energy polarimeter [1]. The beam enters the detector from the lower left side and hits a target at the center. The outgoing particles are detected by scintillators to the left, to the right, above and below the beam line.

2 New Read-Out Sytem

The present read-out electronics consists of analogue NIM modules. Its ability to provide online data is limited by dead time and pileup separation. To improve performance and keep the polarimeter operational in the future the read-out system will be replaced by a new one using field programmable gate arrays (FPGA).

The new read-out system will make use of the so-called GANDALF VME-module [2] developed for the COMPASS experiment at the university of Freiburg. GANDALF uses two analog to digital converter mezzanine cards, which have a total of eight input channels at a sampling rate of 1 GHz and a resolution of 12 bits. Two such modules can analyze all twelve output channels. The signals can be processed on the board using an FPGA. The input data can be analyzed continuously as it is measured, eliminating dead time.

As in the current read-out, the pulse height and the time between the detector hits will be used for event selection. Both time and amplitude are measured by a discrete constant fraction discriminator implemented on the board. The timing resolution of the electronics is in the order of 50 ps.

The polarimeter will also be used to examine scattering reaction of deuterons off proton or carbon targets at a kinetic energy of 75 MeV. The cross section, vector and tensor analyzing powers will be measured.

*IKP Forschungszentrum Jülich, Germany

References

[1] M. Eggert: Entwicklung eines gepulsten Casium-Ionenstrahls fur die Quelle polarisierter Ionen an COSY/Julich, Ph.D. Thesis

[2] S. Schopferer et al. : Development and Performance Verification of the GANDALF High-Resolution Transient Recorder System, IEEE Transactions on Nuclear Science, vol.58, no.4, pp.1456-1459, Aug. 2011

Data Interface between COSY and EDDA-DAQ System

F. Hinder[a,b], V. Hejny[a], M. Simon[a] and P. Wüstner[c] for the JEDI collaboration

The precursor experiments towards an EDM (Electric Dipole Moment) search at a storage ring, aimed by the JEDI (Juelich Electric Dipole moment Investigations) collaboration, requires tools to control the spin motion in storage rings with an absolute high precision. In the year 2014 studies towards the lengthening of Spin-Coherence-Time, systematic analysis of spin imperfections, the commissioning of a Radio-Frequency-Wien-Filter and high precision measurements of the spin tune were performed [1, 2, 3, 4, 5]. All these studies correlate the polarisation measurements, done with the EDDA detector, with the settings of the storage ring COSY (COoler SYnchrotron).

Until now the settings of COSY are stored in one database and the EDDA data are stored in a second database, with the date and time as synchronisation. Both information are in two different, not connected networks. For an easier handling of COSY settings a new connection between both systems, COSY control system and EDDA-DAQ, was designed. The used protocol to transport the data from COSY to EDDA is the MQTT protocol (Message Queue Telemetry Transport) [6]. To implement the protocol a server, connected to the COSY network and the EDDA network was installed. A sketch of the network is given in figure 1. All subsystems of COSY, like Beam Position Monitors (BPMs), tune measurements, Beam Profile Monitors, COSY control software etc. connect themselves to the server as a client and transmit their measurements to it. The EDDA-DAQ system subscribes as a client to the server, receives all available data and writes them to disk. The synchronisation with the EDDA detector is ensured by the synchronisation of the system time of all involved systems.

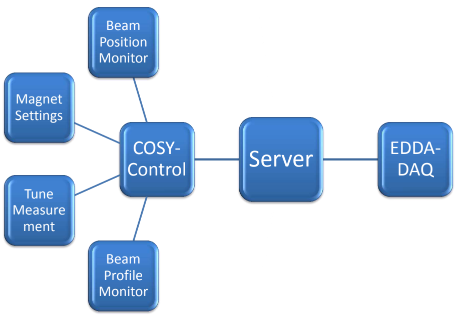

Fig. 1: Connection between COSY control software, the MQTT Server and the EDDA-DAQ system.

As an example the COSY BPM system measurements are discussed: During the measurement series of varying the strength of two solenoids in COSY to detect spin tune changes [2], the BPM system measured every 5 s the orbit of the particle beam. A measurement of the vertical orbit of BPM 8 is shown as an example in figure 2. During the time interval 100 s$< t <$ 125 s the 2 MeV cooler solenoid and the compensation solenoid were switched from their nominal strength to a new strength. The nominal strength of the 2 MeV cooler is 0%, the one of the cooler solenoid is 182 A. The change of the strength of the two solenoids lead to a change of the orbit of the particle beam at the BPM position of $\Delta_{bpmy8} = 0.208 \pm 0.041$ mm. The difference of the mea-

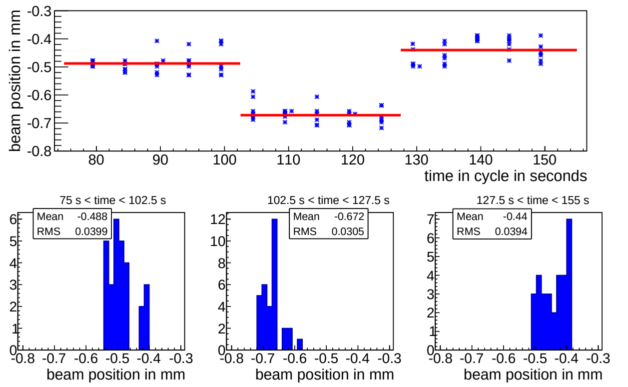

Fig. 2: Measured beam position with the vertical BPM 8. In the time interval $t \in [100s, 125s]$ the 2 MeV cooler solenoid was switched from 0% to 50% and the compensation solenoid was switched from 182 A to 152 A. The orbit change is calculated by the mean and RMS values in the three time intervals (bottom plots).

sured beam position can be calculated for every beam position monitor around the COSY ring. A global variation of the particle orbit can be calculated by averaging all horizontal and vertical beam position measurements:

$$\Delta_x = \frac{\sum_{BPM(x)} |\Delta_{x_i}|}{N_{BPM(x)}} \qquad \Delta_y = \frac{\sum_{BPM(y)} |\Delta_{y_i}|}{N_{BPM(y)}} \tag{1}$$

The goal of the variation of the two solenoids was the measurement of spin tune changes due to solenoidal fields. In addition to the change of the solenoid fields, a change of the beam orbit leads to spin tune changes. To get an estimation of the orbit change due to the field, the beam position measurement values can be used. In figure 3 the measured orbit changes for the variation of the compensation solenoid from 17 A to 197 A is shown. The 2 MeV cooler solenoid is set to 0%. The data show clearly, that the variation in the orbit is compatible with 0 for the currents between 120 A and 200 A. Below 120 A the orbit changes significantly and the change has to be considered as a systematic effect in the spin tune map.

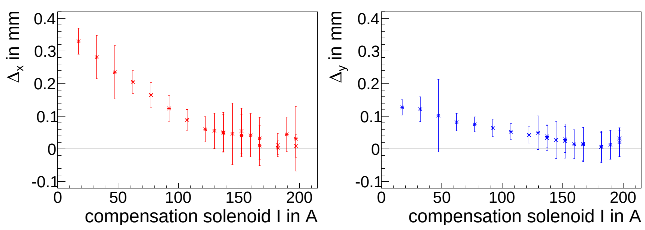

Fig. 3: Change of the orbit due to the change of the magnetic field in the compensation solenoid. (Left: horizontal orbit, Right: vertical orbit).

The BPM measurement is only one example of the implemented MQTT system. In addition, measurements of other COSY systems can now be accessed directly inside the used analysis framework of the EDDA DAQ system. Future systems, which are until now not connected to the MQTT server, can be added easily by implementing a client, which sends the measured data to the server. The EDDA-DAQ system will store the transmitted data automatically and synchronised.

References:

[1] Greta Guidoboni, Spin Coherence Time Measurements at COSY, IKP Annual Report 2013

[2] Arteem Saleev SolenoidChanges

[3] Sebastian Mey WienFilter

[4] Dennis Eversmann SpinTune measurements

[5] JEDI Highlight annual report

[6] MQTT Version 3.1.1. Edited by Andrew Banks and Rahul Gupta. 29 October 2014. OASIS Standard. http://docs.oasis-open.org/mqtt/mqtt/v3.1.1/mqtt-v3.1.1.html

a Institute for Nuclear Physics, FZ Jülich, Germany

b Physics Institute III B, RWTH Aachen University, Germany

c Zentralinstitut für Engineering, Elektronik und Analytik (ZEA), FZ Jülich, Germany

Beam Position Monitors for the HESR

C. Böhme, V. Kamerdzhiev and F. Klehr

In preparation of the High Energy Storage Ring (HESR) within the FAIR-project detailed specifications for a number of beam diagnostic devices have to be prepared. Among the beam diagnostic devices envisaged for the HESR, the beam position monitor (BPM) is considered the most time critical. This is the case because the foreseen location of the BPMs in the arcs, where most of the BPMs are located, affects the design of other components, which have to be ordered soon. The required accuracy is specified to be at least 100 μm. 44 of the 76 BPMs are foreseen to be mounted in the arc sections where lack of space puts additional constraints on the design. This is shown in the overview drawing (Figure 1).

BPM Design Considerations

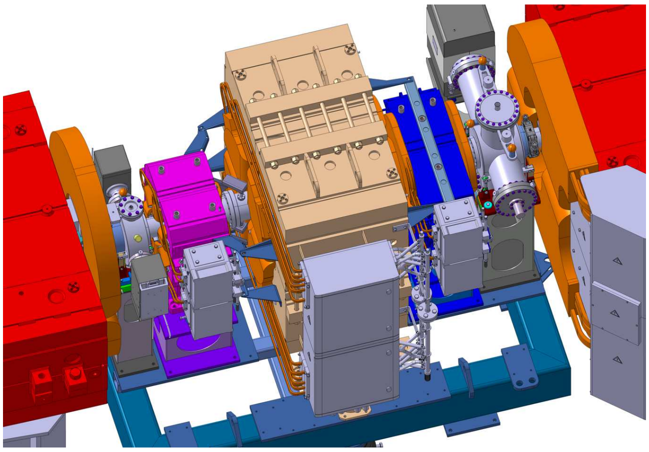

Fig. 1: Overview of the HESR sections between two dipole magnets. The BPM is located between the quadrupole magnet (yellow ochre) and the sextupole magnet (purple), partly reaching into the sextupole magnet.

The inner diameter of the BPM is limited to a minimum of 89 mm and the outer diameter of the beam pipe is limited to 128 mm by the sextupole aperture (Figure 2). When calculating the output signal, the signal amplitude is, among other parameters, dependent on the electrode capacitance to ground. Due to the restrictions of the inner and outer diameters, the capacitance can only be reduced to a certain limit. Therefore, a longer pick-up would also result in a higher capacitance, increasing the total signal amplitude only marginally. With the given worst-case beam parameters, a beam consisting of 10^7 anti-protons in a barrier-bucket, resulting in a 517.5 m long bunch, the signal amplitude would be about $3 \cdot 10^{-6}$ V. Doubling the length of the electrode to 154.4 mm would increase the signal to $3.54 \cdot 10^{-6}$ V, the result would be an increase

Charge	Stored Part.	Bunch Length	Exp. Signal
1	10^7	517.5 m	$3 \cdot 10^{-6}$ V
1	10^7	150 m	$1 \cdot 10^{-5}$ V
1	10^{11}	517.5 m	$3 \cdot 10^{-2}$ V
92	10^{11}	150 m	10 V

Table 1: Calculated signal levels for different beam modes.

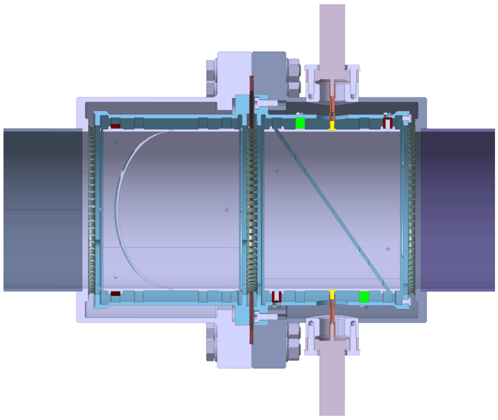

Fig. 2: Design concept of a foreseen BPM pick-up assembly for both plains. Each assembly for one plain has a length of 77.2 mm and an inner diameter of 89 mm.

of only 17%. The presented considerations show that longer BPM electrodes would not significantly improve the signal.

Clearing of Trapped Residual Gas Ions

In case of an anti-proton beam, ions, formed by the interaction of the beam with the residual gas, are trapped in the beam potential [1]. Beyond a certain ion number this can lead to e.g. emittance growth or beam instabilities. The threshold is determined by several factors. On one hand the production rate, which is determined by the amount of stored particles, the revolution frequency and the residual gas pressure. On the other hand the depth of the trapping potential, determined by the amount of stored particles, which determines if the thermal ions can escape the potential. In order to avoid the adverse effects the residual gas ions should be cleared out of the beam. This can be done using an electric field. Due to lack of free space in the arcs one could use one pair of BPM electrodes to generate this field.
This approach can result in additional signal degradation because of the necessary protection electronics for the preamplifiers or residual gas ions hitting the electrodes. On the other hand the clearing system is only needed under some conditions, as explained above. In the first years of operation this threshold will probably not be reached. Additionally, NEG coating of the vacuum pipes to lower the residual gas pressure will be applied to reduce the ion production rate. In order to implement the ion clearing system using the BPM electrodes only the electronics outside the vacuum system will have to be changed. Because of this, the ion clearing can be implemented at a later stage.
At the location of the PANDA detector poor vacuum conditions due to target operation and the small beam size are expected to lead to a high number of residual gas ions being trapped. However, this issue will have to be resolved with other devices than the BPM electrodes.

References:

[1] **Hinterberger, F.**, *Ion Trapping in the High-Energy Storage Ring HESR*, University of Bonn, 2011

Upgrade of the beam profile monitoring system in the COSY IBL

K. Reimers, V. Kamerdzhiev

The injection beam line (IBL) of COSY consists of 4 straight and 4 bent sections. At the beginning and at the end of each bent section a profile grid (also known as SEM Grid) [1] station is used to measure the position and profile of the ion beam delivered by the cyclotron 'JULIC' to COSY. Each of the 8 stations contains a horizontal and a vertical profile grid (PG) assemblies installed in a vacuum chamber. Each PG is made of 39 wires and can be moved in or out of the beam by means of pneumatic drives. The profile data is used primarily to optimize the beam line transmission. Further maintenance of the outdated PG readout electronics is considered impractical. A decision was made to upgrade the system with the state of the art multichannel readout modules, designed and built by iThemba LABS, South Africa. Similar readout electronics was previously used at COSY for the LPM project [2].

An ARM-Processor-based Beaglebone microcomputer running Ubuntu 13 reads out the integrator chips and provides Ethernet connectivity. Each module can readout up to 48 channels of low current sources simultaneously and broadcast the data using an EPICS environment . Each PG is now read out by a dedicated pico amperemeter module, requiring 16 modules for all 8 PG stations. 2 PG stations are located in the cyclotron bunker, the other 6 stations are located inside the IBL hall. The injection of H^-,D^- ions is synchronized with 20 ms macro pulses at a maximum frequency of 0.5 Hz. 16 modules have been put into service. Each module connects to a corresponding PG via 39 double shielded coaxial cables. The readout modules are mounted pairwise underneath the PG stations to keep the analogue lines as short as possible. The distance to the control room is bridged by the TCP/IP based network using standard industrial components. This approach delivers very smooth signals in both continuous and triggered mode.

The measured beam profiles are shown in the GUI in the accelerator control room. The GUI also provides all means to interact with the hardware. Measurement sensitivity, trigger mode and position of the PG (in or out), can be set. A feature to take a reference curve is provided for each PG. The new system was successfully used to optimize the IBL during the recent runs with polarized and unpolarized H^- beams. The system utilizes a distributed architecture having a dedicated readout module for each PG. This results in a capability to perform truly simultaneous measurements with all 16 PG. This feature turned out to be very useful. The tests also revealed occasional loss of network connection. In the cyclotron bunker (PG stations 1 and 2) this behavior can be explained by high radiation background especially during irradiation runs when a target is being irradiated by a dc beam inside the cyclotron bunker. This mode of operation required an additional radiation shielding for the readout modules. For other PG this behavior is proven to be caused by firmware issues and is observed very rarely.

Long term testing is still to be performed to evaluate the reliability and availability of the new system.

Despite some minor issues which are being resolved, the new PG readout system is operational. It has been successfully used to measure the beam profiles and perform fine tuning of the COSY injection beam line.

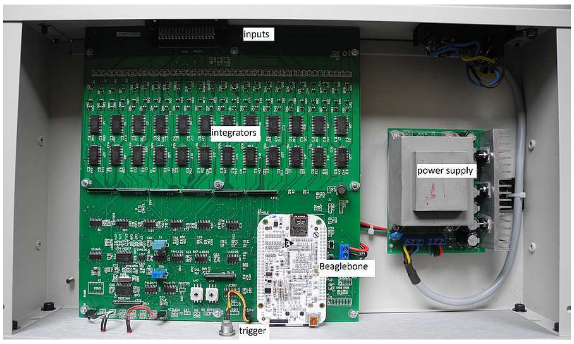

Fig. 1: Inside of the multichannel pico amperemeter module. The white PCB is the BEAGLEBONE providing TCP/IP connectivity.

Fig. 2: PG4.1 in the COSY IBL. Below the cable duct the new readout electronics is installed.

References:

[1] **G.W. Tautfest and H. R. Fechter,**, *A Nonsaturable High Energy Beam Monitor*, Rev. Sci. Instr. 26, 229 (1955)

[2] **Böhme, C.**, *Untersuchungen zur Profilmessung von Hadronenstrahlen mittels Restgaslumineszenz und -ionisation*, Technical University Dortmund, 2011

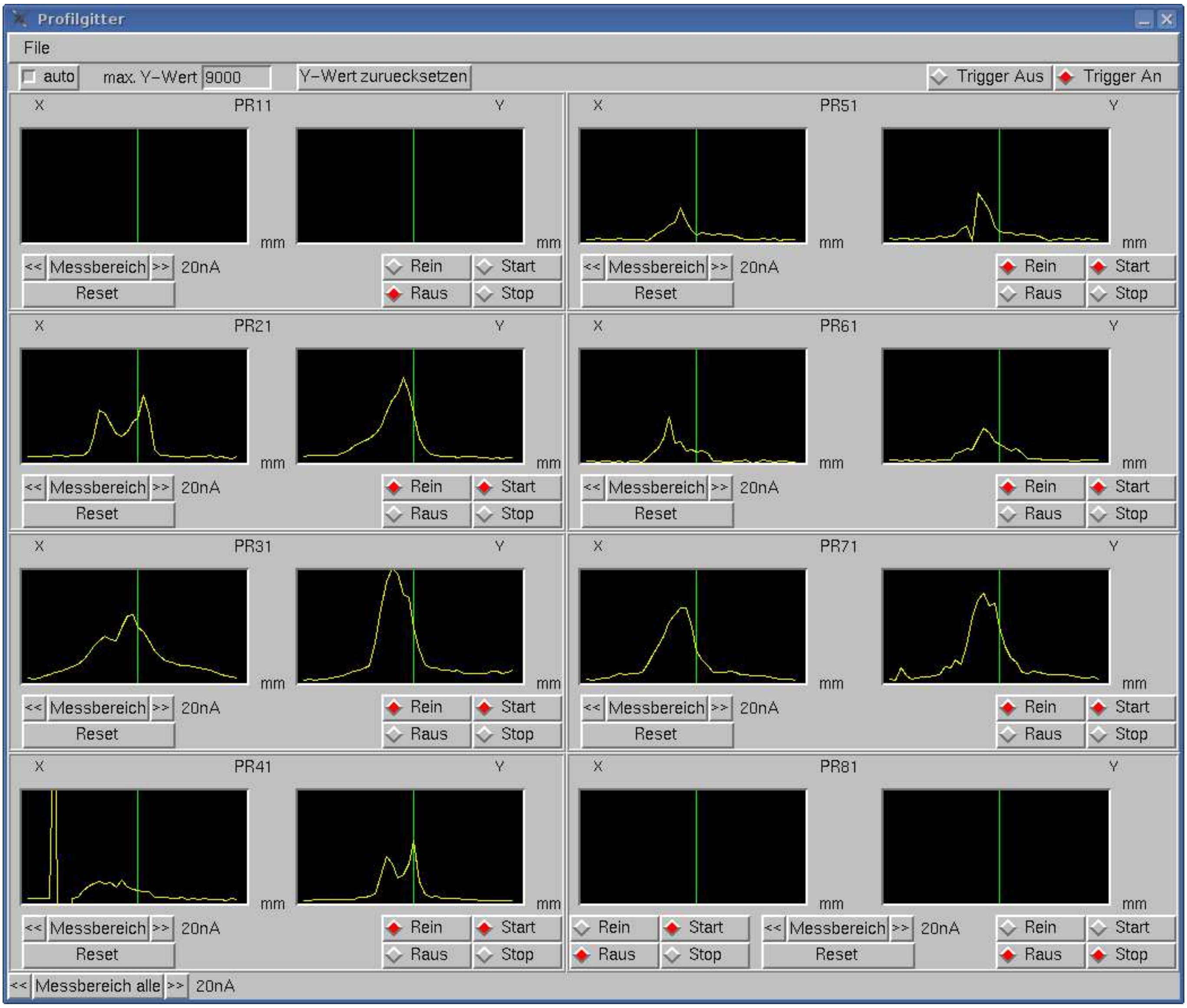

Fig. 3: First profile measurements in the IBL using the new readout modules. PG stations 1 and 8 were not equipped with the read out modules during the measurement.

Automated Compensation of Larmor Rotation in the 2 MeV Electron Cooler

A.Halama

The 2 MeV electron cooler has been installed in the COSY ring in 2013 for cooling the proton and deuteron beams in the entire energy range of the machine and to gather knowledge for a proposed 4/8 MeV cooler at the HESR (FAIR) [1].

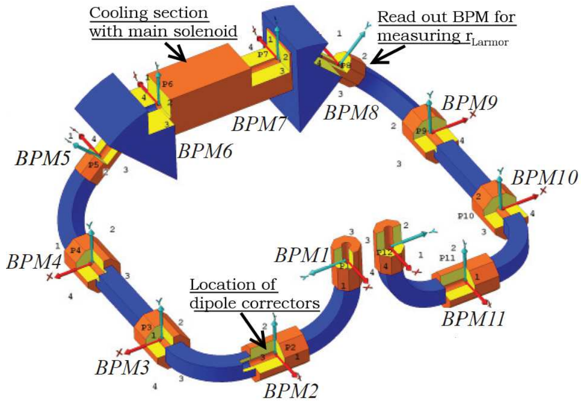

Fig. 1: Electron beam line of the 2 MeV cooler.

Beam Line Adjustment

The electron beam is guided by a longitudinal magnetic field, which allows a lossless transition while keeping the low electron beam temperature. This is important for a high cooling efficiency and suitable recuperation conditions. The wide energy range of 25 keV to 2 MeV [1] and the given geometry make manual adjustments of the beam line time consuming. For that reason slightly mismatched settings of the magnetic elements may remain during operation, which affect the beam as localized heating effects i.e. transverse kicks. Given the magnetic guiding field, a transverse velocity yields a helical trajectory, which is called the larmor rotation. A thusly heated beam is incapable of cooling and may even disturb COSY operations.

In order to deliver a suitable electron beam for cooling the beam's orbit and a small larmor radius inside the cooling section are of great importance. The first objective is dealt with manually using a limited number of orbit correctors. The latter is achieved by an optimal setting of a pair of short dipoles (EDIPs), highlighted in Figure 1. A properly designed kick by the EDIPs may compensate the disturbing transverse velocity component of the beam. To find that setting, an automated procedure to compensate the larmor rotation has been developed and tested successfully.

Automated Compensation of the Larmor Rotation

The larmor radius quantifies the larmor rotation and must be measured. Therefore beam positions are logged using BPM 8, pointed at in fig. 1, while the current of the main solenoid is varied. Since an increase of the magnetic induction compresses the larmor spiral, changes of the larmor phase are measured at one stationary BPM. A numeric analysis of the collected data yields the larmor radius. To obtain the relation between the settings of the EDIPs and the resulting larmor radii, the mentioned procedure is repeated with varying EDIP settings. A theoretical model, which predicts a larmor radius of 0 μm at the ideal dipole setting, is used to approach the best possible setting. The model is shown in the following graph.

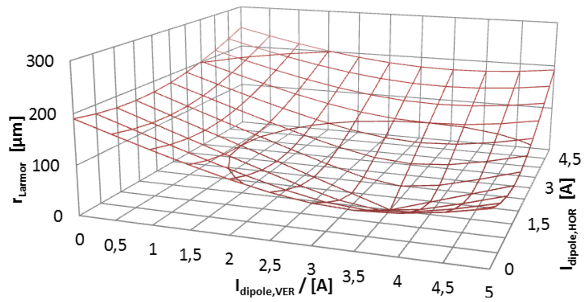

Fig. 2: Experimentally verified model of the correlation of the EDIP setting and the resulting larmor radius.

Given a set of measured correlations a two-dimensional linear regression leads to an optimized dipole setting. Since measurement accuracy is limited, the obtained result is an approximation of the ideal dipole setting. The procedure is repeated, each starting at the last known optimized dipole setting. The automated procedure has been tested successfully and provides time savings of earlier 1 hour of manual adjustment to now 8 to 15 minutes with even more precise results. Exemplary measurements of the larmor radius in an uncompensated and a compensated case are shown in fig. 3.
The next step towards the automated adjustment of the cooler is to work with a model that utilizes more beam line data and properties of all influencing magnetic elements. That will allow for adjustment of all magnetic elements to find optimized solutions for the orbit and larmor rotation in the entire beam line.

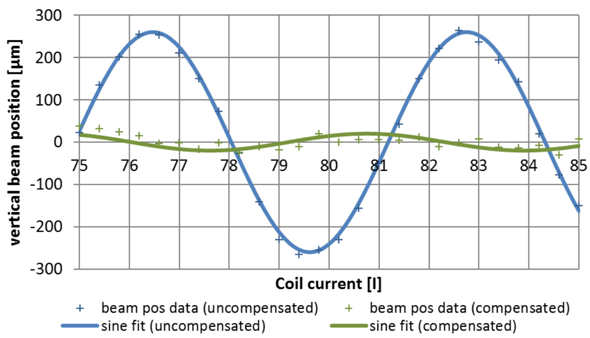

Fig. 3: Electron beam position at BPM 8 vs. the current of the main solenoid. The automated compensation led to the larmor rarius of 20 μm compared to 260 μm in the uncompensated case.

Acknowledgement:
The author is most grateful for the advice and fruitful discussions with V. Reva, M. Bryzgunov and V. Kamerdzhiev. Thanks to the COSY team for their support.

References:

[1] **Alinovskiy, N. et al.**, *2MeV Electron Cooler for COSY and HESR - First Results*, IPAC2014

An RF Wien-filter for EDM Searches at COSY

Sebastian Mey[*†] and Ralf Gebel[*] for the JEDI Collaboration

1 Motivation

The motion of a relativistic particle's spin in an electromagnetic storage ring ($\vec{\beta}\cdot\vec{B}=0$) with non vanishing EDM contributions is given by the generalized *Thomas-BMT* Equation[1], $\mathrm{d}\vec{S}/\mathrm{d}t=\vec{S}\times(\vec{\Omega}_{\mathrm{MDM}}+\vec{\Omega}_{\mathrm{EDM}})$, with

$$\begin{aligned}\vec{\Omega}_{\mathrm{MDM}} &= \frac{q}{m}\left((1+\gamma G)\vec{B}-\left(\gamma G+\frac{\gamma}{\gamma+1}\right)\vec{\beta}\times\frac{\vec{E}}{c}\right)\\ \vec{\Omega}_{\mathrm{EDM}} &= \frac{q}{m}\frac{\eta}{2}\left(\frac{\vec{E}}{c}+\vec{\beta}\times\vec{B}\right)\end{aligned} \tag{1}$$

Here the anomalous magnetic moment G is given by the particle's **M**agnetic **D**ipole **M**oment (MDM), $\vec{\mu}=2(G+1)\frac{q\hbar}{2m}\vec{S}$. This corresponds to $G=-0.142$ for deuterons. As an analogue, the dimensionless factor η describes the strength of the particles permanent **E**lectric **D**ipole **M**oment (EDM) relative to its MDM. For a Standard Model prediction of $d=\eta\frac{q\hbar}{2mc}\vec{S}\approx 10^{-30}\,\mathrm{ecm}$ its value is $\eta\approx 10^{-15}$.
In a purely magnetic storage ring, all the terms containing electric fields in Eq. 1 vanish and the EDM contribution due to the interaction with the motional electric field ($\vec{\beta}\times\vec{B}$) will lead to a tiny tilt of the spin's precession axis. This leads to a very slow oscillation of the vertical polarization, but for $\eta\approx 10^{-15}$ its contribution is far below measurable. Adding an RF *Wien*-Filter with vertical magnetic field orientation to the ring's lattice yields a modulation of the horizontal spin precession by means of a phase kick. Together with the EDM's interaction with the motional electric field in the rest of the ring, this frequency modulation results in a continuous buildup of vertical polarization in a beforehand horizontally polarized beam.[2]

2 Setup of the Prototype

While the above described approach could provide a measurable EDM signal, it doesn't yield a clear observable to characterize the RF *Wien*-Filer itself. Therefore, a first prototype where a radial magnetic field ($\vec{B}=(B_x,0,0)^T$) is compensated by a vertical electric field ($\vec{E}=(0,E_y,0)^T$) has been commissioned. The dipole fields then directly apply torque onto the vertical component of the polarization vector. In the case of *Lorentz* force cancellation, the device is entirely EDM transparent. Expressing the electric field in Eq. 1 in terms of the magnetic field leads to a simple formula for the spin precession in a *Wien*-Filter[3]:

$$\vec{\Omega}=\frac{q}{m}\left((1+\gamma G)\vec{B}-\left(\gamma G+\frac{\gamma}{\gamma+1}\right)\beta^2\vec{B}\right)=\frac{1+G}{\gamma}\vec{B}. \tag{2}$$

The particles sample the localized RF fields of the *Wien*-filter once every turn. Their contribution may be approximated by the integrated field along the particles' path assigned to a point-like device at an orbital angle θ:

$$b(\theta)=\int\hat{B}_x\,\mathrm{d}l\,\cos(f_{\mathrm{RF}}/f_{\mathrm{rev}}\theta+\phi)\sum_{n=-\infty}^{\infty}\delta(\theta-2\pi n). \tag{3}$$

The resonance strength $|\varepsilon_K|$ of such a device is given by the amount of spin rotation per turn and can be calculated by the *Fourier* integral over one turn in the accelerator[5, 6]:

$$\begin{aligned}|\varepsilon_K| &= \frac{f_{\mathrm{spin}}}{f_{\mathrm{rev}}}=\frac{1+G}{2\pi\gamma}\oint\frac{b(\theta)}{B\rho}e^{iK\theta}\,\mathrm{d}\theta\\ &= \frac{1+G}{4\pi\gamma}\frac{\int\hat{B}_x\,\mathrm{d}l}{B\rho}\sum_n e^{\pm i\phi}\delta(n-K\mp f_{\mathrm{RF}}/f_{\mathrm{rev}}).\end{aligned} \tag{4}$$

An artificial spin resonance occurs at all side-bands with a frequency corresponding to the spin tune:

$$K\overset{!}{=}\gamma G=n\pm f_{\mathrm{RF}}/f_{\mathrm{rev}}\ \Leftrightarrow\ f_{\mathrm{RF}}=f_{\mathrm{rev}}|n-\gamma G|;\ n\in\mathbb{Z}. \tag{5}$$

In the scope of the current JEDI experiments (**J**ülich **E**lectric **D**ipole Moment **I**nvestigations), deuterons with a momentum of 970 MeV/c are stored at COSY. In this case, $\gamma=1.126$ and the resulting spin tune is $\gamma G=-0.1609$. The fundamental mode is located at $f_{\mathrm{RF}}=121\,\mathrm{kHz}$ with $n=\pm 1$ harmonics at 629 kHz and 871 kHz.
The magnetic RF dipole has been realized in the form of coil wound lengthwise around a ceramic part of the beam-pipe. It is driven by means of a parallel resonance circuit with a quality factor of $Q\approx 20$. A similar but separate resonance circuit drives the electric RF dipole. The electric field is generated by the potential difference between two stainless steel electrodes inside the vacuum chamber. A detailed description of the setup can be found in the highlights of the IKP/ COSY annual report 2013.[4]
Without any additional control loops and further dedicated cooling systems it is possible to run the system up to 90 W input power in continuous, long term operation. The corresponding operating parameters have been collected in Table 1.

Parameter	RF B dipole	RF E dipole
$\hat{U}$		2 kV
$\int\hat{E}_y\,\mathrm{d}l$		24.1 kV
$\hat{I}$	5 A	
$\int\hat{B}_x\,\mathrm{d}l$	0.175 T mm	
freq. range	630 kHz to 1170 kHz	630 kHz to 1060 kHz

Table 1: The RF $E\times B$ dipole at 90 W input power.

Fig. 1 shows the distribution of the main component of the *Lorentz* force. Due to different drop-off rates of the electric and magnetic field, particles will encounter a down-up kick at the entrance and a corresponding up-down kick at the exit of the *Wien*-Filter, but the geometry has been optimized insofar that for particles entering the system on axis, the integrated *Lorentz* force along the beam path is set to zero.

3 Measurements

To achieve *Lorentz* force cancellation, the phase as well as the amplitudes of the E and B fields have to be adjusted. The accelerator optics was modified so that a vertical betatron sideband was shifted exactly on top of the frequency of

*IKP, Forschungszentrum Jülich GmbH, Germany
†III. Physikalisches Institut B, RWTH Aachen, Germany

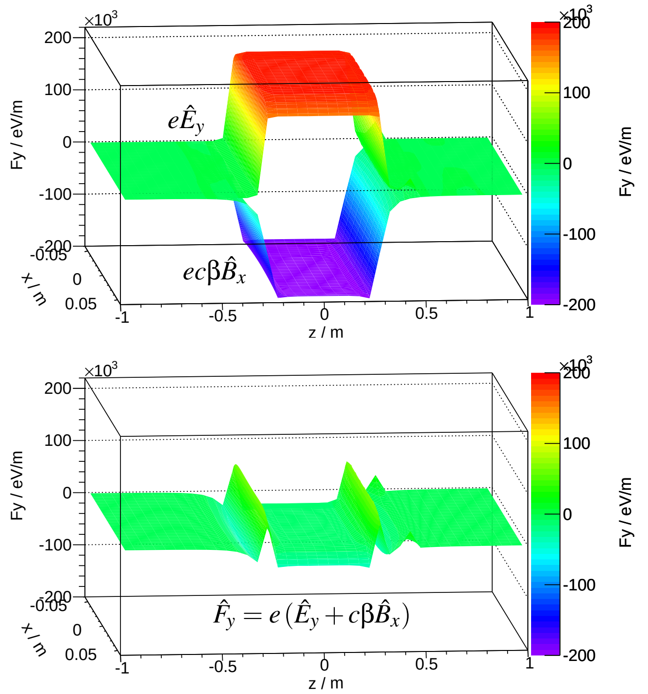

Fig. 1: Simulation of the *Lorentz* force on a particle entering the RF $E \times B$ dipole on axis plotted across a horizontal cut through the center of the beam pipe ($y = 0$). The results have been normalized to a coil current amplitude of $\hat{I} = 1A$.

the RF $E \times B$ dipole at 871.52 kHz to achieve maximum sensitivity to induced beam oscillations. Next, the acceptance was limited by installing a massive carbon block directly above the beam as target for the polarimeter. The beam current monitor of COSY could thus be used as a precise tool for the matching of the RF *Wien*-Filter. With a well cooled beam, a sensitivity to amplitude and phase changes in the per mill regime has been achieved.

For polarimetry runs, the deuteron beam is slowly moved onto the carbon target.[7] Polarization manifests itself in the angular distribution of $^{12}\mathrm{C}(\vec{\mathrm{d}},\mathrm{d})$ scattering. In case of a vertical polarized beam, this leads to an asymmetry in the event rates of the left and right quadrants of the polarimeter detector.

The RF $E \times B$ dipole was operated for 30 s per fill. Spin-kicks every turn lead to an adiabatic rotation of the polarization vector, corresponding to an oscillation of its vertical component, in turn represented by the left-right cross-ratio CR_y in Fig. 2. A complete spin flip occurs only for an exact match between the exciting RF frequency and the spin resonance frequency, otherwise the excitation will slip beneath the precessing spin, accompanied by an increase in oscillation frequency. This allows the determination of the spin resonance frequency down to ≈ 0.01 Hz with a series runs scanning the tip of the resonance curve (see right panel of Fig. 2). The frequency of the driven oscillation on resonance is directly proportional to the resonance strength (see Eq. 4).

A series of such scans have been taken during the September 2014 JEDI beam time at COSY to determine the dependence of spin resonance strength upon the betatron tune. Once the *Wien*-Filter was matched at coinciding betatron and spin resonance side bands, the optics of the accelerator was moved towards different vertical betatron frequencies. For comparison, at each tune similar scans were taken with an already installed RF solenoid and the RF $E \times B$ dipole op-

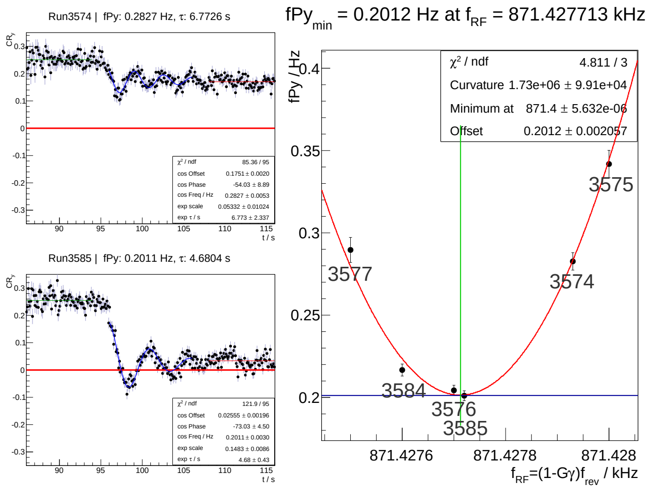

Fig. 2: The left panel shows the damped, driven oscillation of the vertical polarization component in case of excitation slightly off (top) and on resonance (bottom). The right panel shows fitted frequencies from different runs for varying excitation frequencies. The points form the tip of the spin resonance curve.

erated without a compensating electric field. Fig. 3 shows this tune dependency. The matched *Wien*-Filter as well as the solenoid don't excite coherent betatron oscillations. As the simple derivation of Eq. 4 suggests, the resonance strength is indeed independent of the vertical betatron tune. In contrast, the resonance strength of the pure magnetic RF dipole is dominated by the interference between the direct spin rotations and those induced by coherent beam oscillations.

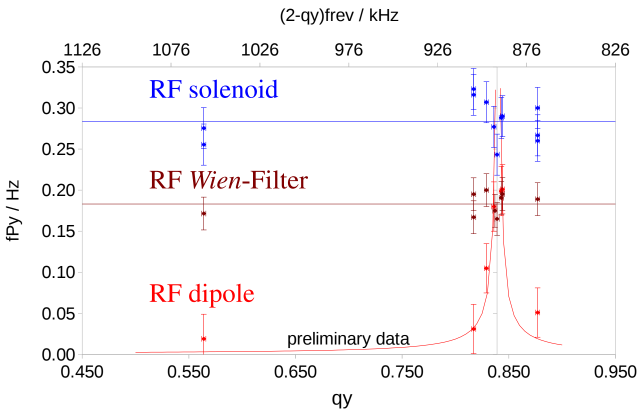

Fig. 3: Resonance strengths for different fractional vertical betatron tunes. The top scale gives the frequency of the betatron sideband, the vertical line at 871 429.00 Hz is the frequency where the betatron sideband coincides with the spin resonance.

4 Conclusion

In preparation for future EDM experiments in storage rings, a first prototype of an RF *Wien*-Filter has been commissioned at COSY. We have shown, that this device fulfills the expectation of generating a configuration of RF dipole fields for spin manipulation without any excitation of coherent beam oscillations.

References:

[1] T. Fukuyama and A. J. Silenko, *Int. J. Mod. Phys. A* **28**, 1350147 (2013).

[2] W. M. Morse, Y. F. Orlov and Y. K. Semertzidis, *Phys. Rev. ST Accel. Beams* **16**, 114001 (2013).

[3] N. N. Nikolaev, `http://www.bnl.gov/edm/files/pdf/NNikolaev_Wien_RFE.pdf`*Duality of the MDM-transparent RF-E Flipper to the EDM transparent RF Wien-Filter at all Magnetic Storage Rings* (2012).

[4] Institut für Kernphysik/ COSY *Juel-4367* (2013).

[5] M. Bai, W. W. MacKay, and T. Roser, *Phys. Rev. ST Accel. Beams* **8**, 099001 (2005).

[6] S. Y. Lee, *Phys. Rev. ST Accel. Beams* **9**, 074001 (2006).

[7] Z. Bagdasarian et al., *Phys. Rev. ST Accel. Beams* **17**, 052803 (2014).